UNIVERSIDADE FEDERAL DE MINAS GERAIS

Escola de Engenharia

Programa de Pós-Graduação em Engenharia Elétrica

Stella Diniz Urban

BIPEDAL WALKING CONSTRAINED CONTROLLER

Belo Horizonte, Brazil
2023

Stella Diniz Urban

BIPEDAL WALKING CONSTRAINED CONTROLLER

Dissertation submitted to the Programa de Pós-Graduação em Engenharia Elétrica of Escola de Engenharia at the Universidade Federal de Minas Gerais, in partial fulfillment of the requirements for the degree of Master in Electrical Engineering.

Advisor: Bruno Vilhena Adorno

Belo Horizonte, Brazil
2023

Urban, Stella Diniz.
U73b Bipedal walking constrained controller [recurso eletrônico] / Stella Diniz Urban. - 2022.
1 recurso online (60 f. : il., color.) : pdf.

Orientador: Bruno Vilhena Adorno.

Dissertação (mestrado) - Universidade Federal de Minas Gerais, Escola de Engenharia.

Bibliografia: f. 51- 60.
Exigências do sistema: Adobe Acrobat Reader.

1. Engenharia Elétrica - Teses. 2. Caminhada – Teses.
3. Programação Quadrática – Teses. I. Adorno, Bruno Vilhena.
II. Universidade Federal de Minas Gerais. Escola de Engenharia.
III. Título.

CDU: 621.3(043)

Ficha catalográfica elaborada pela Bibliotecária Letícia Alves Vieira - CRB-6/2337
Biblioteca Prof. Mário Werneck - Escola de Engenharia da UFMG

UNIVERSIDADE FEDERAL DE MINAS GERAIS
ESCOLA DE ENGENHARIA
PROGRAMA DE PÓS-GRADUAÇÃO EM ENGENHARIA ELÉTRICA

FOLHA DE APROVAÇÃO

"BIPEDAL WALKING CONSTRAINED CONTROLLER"

STELLA DINIZ URBAN

Dissertação de Mestrado subme da à Banca Examinadora designada pelo Colegiado do Programa de Pós-Graduação em Engenharia Elétrica da Escola de Engenharia da Universidade Federal de Minas Gerais, como requisito para obtenção do grau de Mestre em Engenharia Elétrica. Aprovada em 21 de novembro de 2022. Por:

Prof. Dr. Bruno Vilhena Adorno
DEE (UFMG) - Orientador

Prof. Dr. Luciano Cunha de Araújo Pimenta
DELT (UFMG)

Prof. Dr. Guilherme Vianna Raffo
DELT (UFMG)

Documento assinado eletronicamente por **Bruno Vilhena Adorno**, **Usuário Externo**, em 25/11/2022, às 10:39, conforme horário oficial de Brasília, com fundamento no art. 5º do Decreto nº 10.543, de 13 de novembro de 2020.

Documento assinado eletronicamente por **Guilherme Vianna Raffo**, **Professor do Magistério Superior**, em 25/11/2022, às 14:40, conforme horário oficial de Brasília, com fundamento no art. 5º do Decreto nº 10.543, de 13 de novembro de 2020.

Documento assinado eletronicamente por **Luciano Cunha de Araujo Pimenta**, **Professor do Magistério Superior**, em 29/11/2022, às 15:47, conforme horário oficial de Brasília, com fundamento no art. 5º do Decreto nº 10.543, de 13 de novembro de 2020.

A auten cidade deste documento pode ser conferida no site h ps://sei.ufmg.br/sei/controlador_externo.php?acao=documento_conferir&id_orgao_acesso_externo=0, informando o código verificador **1871001** e o código CRC **F7F21FBD**.

I dedicate this thesis to my parents,
Maria Amélia and Gilberto

Acknowledgements

I thank my advisor for all the knowledge he gave me and his patience during these pandemic years. I also thank Juancho for the revisions and corrections of the work and the words of encouragement.

Resumo

Esta dissertação apresenta um método para controlar uma caminhada bípede quasi-estática baseado em programação quadrática e em desigualdades diferenciais usando primitivas geométricas. Permite-se que o centro de massa se mova para qualquer lugar dentro do polígono de suporte durante o ciclo de caminhada, diferentemente dos métodos clássicos, que geralmente dependem do rastreamento de uma trajetória desejada para o ponto de momento zero. As restrições também mantêm o equilíbrio do robô, a pelvis acima de uma altura mínima e evitam a violação dos limites das juntas durante o ciclo completo da caminhada. Os resultados da simulação, usando as pernas do robô humanoid Poppy, mostram que as trajetórias do sistema em malha fechada convergem para a posição desejada do centro de massa durante a fase de suporte duplo e as trajetórias do pé de balanço convergem para a pose desejada durante a fase de suporte simples, enquanto todas as restrições foram respeitadas.

Palavras-chave: Caminhada Bípede, Primitivas Geométricas, Programação Quadrática, Restrições

Abstract

This thesis presents a method to control a quasi-static bipedal walking based on quadratic programming and differential inequalities using geometric primitives. The center of mass is allowed to move anywhere inside the support polygon during the walking cycle, as opposed to classic methods, which usually rely on tracking a desired trajectory for the zero moment point. The constraints keep the robot balance, the pelvis above a minimum height, and prevent the violation of joint limits during the complete walking cycle. Simulation results using the legs of the Poppy humanoid robot show that the trajectories of the closed-loop system converge to the desired center of mass position during the double support phase and the swing foot's trajectories converge to the desired pose during the single support phase while all constraints are obeyed.

Keywords: Bipedal Walking, Geometric Primitives, Quadratic Programming, Constraints

List of Figures

Acronyms

CoM	Center of Mass.
COMAN	Compliant Humanoid Platform.
CoP	Center of Pressure.
DARPA	Defence Advanced Research Projects Agency.
DSP	Double Support Phase.
DFK	Differential Forward Kinematics.
DoF	Degrees of Freedom
FZMP	Fictitious ZMP.
H5	Humanoid 5.
H6	Humanoid 6.
H7	Humanoid 7.
HRP	Humanoid Research Project.
HZD	Hybrid Zero Dynamics.
KAIST	Korean Advanced Institute of Science and Technology.
KRH	KAIST Humanoid Robot.
MACRO	Research Group on Mechatronics, Control and Robotics.
NASA	National Aeronautics and Space Administration.
UFMG	Universidade Federal de Minas Gerais.
VREP	Virtual Robot Experimental Platform.

SDR	Sony Dream Robot.
SP	Support Polygon.
SSP	Single Support Phase.
T-RH	Toyota Humanoid Robot.
ZMP	Zero Moment Point.
WABOT	Waseda Robot.
WL	Waseda Legs.

Notation

$\mathbb{H}$	The set of quaternions.
$\mathcal{H}$	The set of dual quaternions.
$\boldsymbol{h}, \boldsymbol{x}, \boldsymbol{y}$	Quaternions.
$\underline{\boldsymbol{h}}, \underline{\boldsymbol{x}}, \underline{\boldsymbol{y}}$	Dual quaternions.
$\boldsymbol{h}^*$	Quaternion conjugate.
$\underline{\boldsymbol{h}}^*$	Dual quaternion conjugate.
$\overset{+}{\boldsymbol{H}}_4, \overset{-}{\boldsymbol{H}}_4$	Hamilton operators.
$\overset{+}{\boldsymbol{H}}_8, \overset{-}{\boldsymbol{H}}_8$	Hamilton operators extended for dual quaternions.
$\hat{\imath}, \hat{\jmath}, \hat{k}$	Quaternion units.
$\boldsymbol{J}$	Jacobian matrix.
$\boldsymbol{J}_d$	Distance Jacobian matrix.
$\boldsymbol{q}$	Joint vector.
$\dot{\boldsymbol{q}}$	Joint velocity vector.
$\|\underline{\boldsymbol{x}}\|$	Dual quaternion norm.
ε	Dual unit.
η	Scalar gain of the control law.
λ	Damping factor in the optimization problem.
ϕ	Rotation angle.
$\boldsymbol{W}$	Inequality constraints matrix in the optimization problem.

$\boldsymbol{w}$	Inequality constraints vector in the optimization problem.
$\boldsymbol{W}_{\text{eq}}$	Equality constraints matrix in the optimization problem.
$\boldsymbol{w}_{\text{eq}}$	Equality constraints vector in the optimization problem.
η_d	Derivative gain used in the vector field inequalities.
$\boldsymbol{x}$	Task-space vector.
$\boldsymbol{x}_d$	Desired task-space vector.
$\tilde{\boldsymbol{x}}$	Task error.

Sumário

1 Introduction

Humankind is constantly moving forward. We evolved from hunters and collectors to farmers and later to an industrial workforce and scientists (Harari, 2018). One of the products of this evolution is the development of science and technology, which helped us define our modern world. The improvement of medical care, transportation, food production, safety, and leisure, among other amenities, are examples of how technology affects us. The study and invention of automatic devices are examples of how far science has led us. We can see this advance from the development of mechanical devices to the advancement of control theories and later, automation of machines (Guarnieri, 2010) and creation of robots. Humans have imagined automatic structures since the 15th century. Leonard da Vinci, for instance, studied anatomical structures and created many robotic devices such as the first documented articulated humanoid robot (Pasek, 2014), the da Vinci's knight.

During the 1980s, the study of robots intensified and industrial automation was developed (Spong et al., 2006). Industrial robots allowed humans to stop working on repetitive tasks that could harm them (Lundberg et al., 1989; Barr et al., 2003). The development of robots also allowed humans to reach dangerous environments (Davids, 2002; Ko & Lau, 2009; Murphy et al., 2013), assisted disabled people and the elderly (Ishii et al., 1995; Kang et al., 2005; Sales et al., 2016), and assisted doctors in minimally invasive surgeries (Adhami & Coste-Manirei, 2003; Bertelsen et al., 2013; Bergeles & Guang-Zhong Yang, 2014). Additionally, robots explored inhospitable places such as the Moon (Wilcox et al., 2007; Nagaoka et al., 2008), Mars (Volpe et al., 1996; Tarokh et al., 1999), and

the bottom of the ocean (Whitcomb et al., 2000; Yoerger et al., 2000). In the following decades, scientists have built many different types of robots such as manipulator arms (Moran, 2007), aerial robots (Newcome, 2004), wheeled robots (Siegwart et al., 2004), and legged robots (Todd, 1985). Legged robots, for instance, were inspired by legged animals such as spiders (Vidoni & Gasparetto, 2011), dogs (Raibert et al., 2008), and humans (Hirai et al., 2007). Among the many types of robots, the most familiar to people is the humanoid robot due to its resemblance to the human body (Mori et al., 2012).

Humanoid robots have been widely studied for the last thirty years (Yoshida, 2018). The studies have been developed, for instance, first aiming their construction based on a simplification of the human body structures to mechanical limbs (Chevallereau et al., 2009).The human body limbs is composed by many bones, muscles, and tendons. Our lower limbs, for instance, is formed by a group of 11 bones while a humanoid lower structure is usually formed by a pelvis, two thighs, two calves, two feet, and their joints. The studies have also targeted the humanoid modeling, for instance, the kinematic modeling method for a humanoid robot proposed by Oliveira (2015), their gait model based on the Zero Moment Point (ZMP) proposed by Vukobratovic & Juricic (1969), and the first walking implementation on a real humanoid WL-10R using the ZMP method (VUKOBRATOVIĆ & BOROVAC, 2004). Today we see the development of highly complex humanoids able to backflip such as Boston Dynamics Atlas[1].

Since these robots are based on human anatomy, the muscle-skeletal structure of humans is the inspiration to build their actuation system. The robots present a similar number of limbs (thigh, calf, foot), a similar orientation of joints (for instance, the knee joint will bend backward), and joint's limits (similar to human ankles and knees limits). Although lower, compared to humans, the great number of degree of freedom is among the advantages of these robots. Their mobility and their number of degrees of freedom (DoF) allow us the definition of more complex tasks. Atlas, for instance, can walk, run, climb stairs (Kuindersma et al., 2014), perform backflips,[2] and parkour[3].

The elemental task a legged robot can perform is walking. Humans, as shown in Fig. 1.1, train to walk since they are babies, intuitively crawling, then bipedally walking with hands in contact with a vertical surface, to losing one-hand contact, and finally freely walking (Adolph & Robinson, 2013). The robot, however, does not have the same training as humans. Therefore, the walking is simplified as balancing along with the alternate swinging of legs. This simplification brings a challenge: walking is successful if and only if the robot's swinging foot always reaches its desired pose and the whole mechanism does not fall on the floor, i.e., the robot will walk and simultaneously keep its balance.

Many works have addressed the walking challenge using the ZMP concept. The ZMP

[1]https://www.bostondynamics.com/atlas
[2]https://www.youtube.com/watch?v=fRj34o4hN4I
[3]https://www.youtube.com/watch?v=_sBBaNYex3E

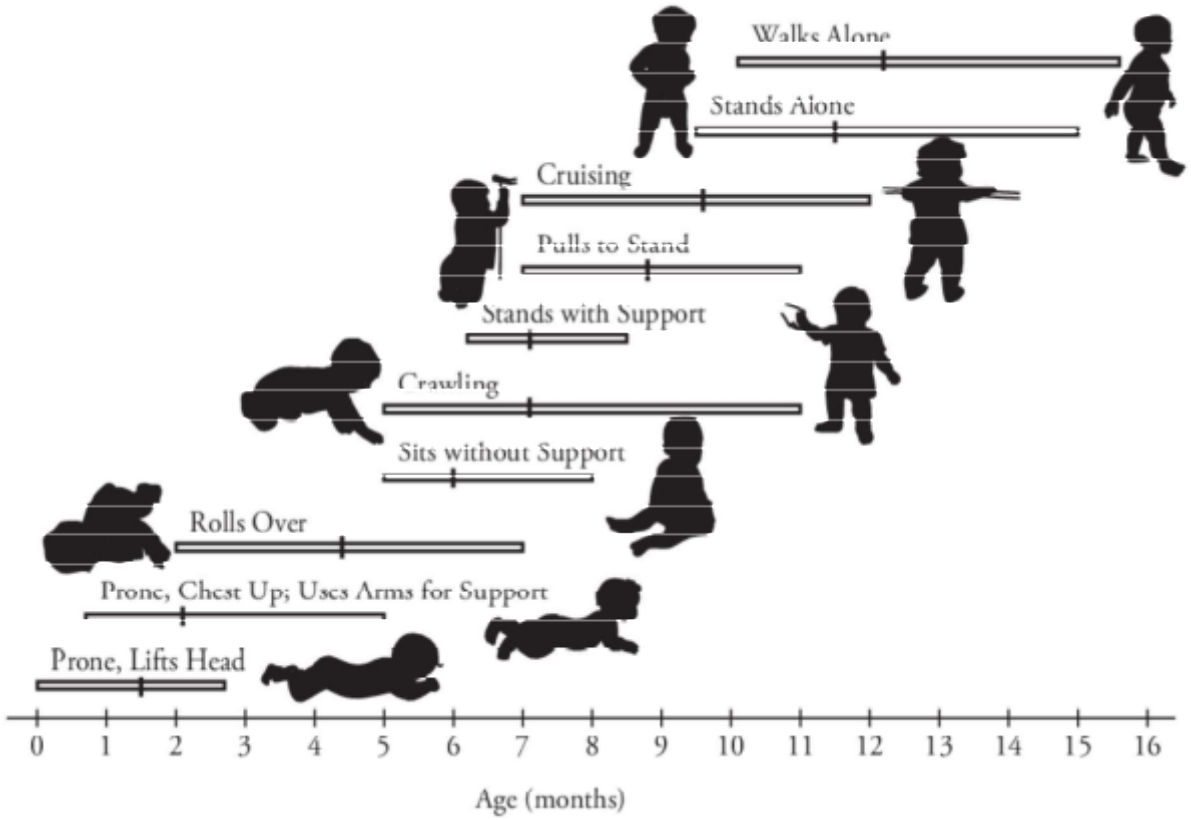

Figure 1.1: Babies' fase of walking development. Image from Adolph & Robinson (2013).

is the point where all active forces can be reduced to a single resultant as well as the point where the horizontal components of the resultant moment are zero (Vukobratovic & Juricic, 1969; VUKOBRATOVIĆ & BOROVAC, 2004). The common characteristic of these works is the restrictive support area, in which the ZMP reference is a line or a set of lines the robot must follow. Humans do not think while they are walking. We usually swing our legs and transfer our ZMP without following a single trajectory. We can simplify our balance behavior to be inside an area instead of following a set of possible trajectories.

Based on the human walking, we proposed a controller to perform the walking while obeying all the robot's physical and balance constraints. To accomplish that, we used a quadratic programming controller with differential inequality constraints (Marinho et al., 2019). The differential inequality constraints are defined in a way that the solution to those differential inequalities is bounded by decreasing exponential functions and has a smooth behavior when approaching the borders of the constraint. We also defined these constraints based on physical limitations such as joint limits and pelvis minimum height and the balance constraints such as planes and cylinders to delimit the area where the ZMP can be.

1.1 Objective and Contributions

The main objective of this thesis is to present a novel method of bipedal walking control with a less constrained ZMP and a simple implementation.

The general objectives are:

- the robot should be able to perform a balanced gait;
- to increase the robot's ability to remain in balance without constraining the ZMP to a trajectory.

The specific objectives are:

- to define the constraints and surfaces using simple geometric primitives to
  - simplify the support polygon,
  - prevent the robot from squatting too low,
  - prevent the foot from sliding on the floor, and
  - the floor as a plane;
- to use the constraints to define the support phases.

Furthermore, our main contribution to this work is the definition of the constraints in a quadratic problem that enables the containment of the ZMP inside the support polygon in a non-restrictive way, instead of the single trajectory that was proposed by Kajita et al. (2003). For instance, in the double support phase (DSP), the ZMP transfer would be the tracking of a single pre-calculated trajectory using the method of Kajita et al. (2003). However, with our technique, the ZMP just needs to be inside the support polygon, so it can do any trajectory as long as it stays inside the polygon.

1.2 Structure of the Text

This work is divided into seven chapters. Chapter 1 presents a brief introduction regarding the bipedal walking. Chapter 2 shows the state of the art related to humanoids and bipedal walking control techniques. Chapter 3 introduces the mathematical background that shows the dual quaternion representation and the kinematic model. Chapter 4 presents the bipedal walking modeling and presents the main concepts related to the bipedal walking such as DSP, single support phase (SSP), and ZMP. It also shows the modeling of the robot, the center of mass (CoM) model, and defines the constraints for each support phase. The constrained controller for each support phase is shown in Chapter 5, the experiments and results are presented in Chapter 6, and the conclusion and future works are shown in Chapter 7.

1.3 Chapter summary

In this chapter, we presented our introduction. We showed the historical line of the robots from the work of Leonardo da Vinci in its efforts to produce a humanoid automaton to the most modern Boston Dynamics humanoid, Atlas. We also showed brief concepts related to the walking such as the ZMP and the balance. Finally, we showed the objectives, the contributions, and the structure of the thesis.

2

State of the Art

In this chapter, we present a brief history of humanoid robots, showing the iconic robots developed throughout the years in Section. 2.1. We also present the state of the art for bipedal walking in Section. 2.2. The Walking Controllers section is divided into three groups of controllers. The first and more important group of techniques for this work is the ZMP-based controllers in Subsection. 2.2.1, followed by the reduced-order models based controllers in Section. 2.2.2, and finally the hybrid dynamic based controller in Section. 2.2.3.

2.1 History of Humanoid Robots

The history of humanoids is much older than some people think. One might say that robots started appearing very recently in the late 1960s when formal research started. Others may remember the first appearance of the word robot, to define a human-like mechanism used for repetitive tasks, in the play *Rossum's Universal Robots*, written by Carl Capek in 1921 (Fukuda et al., 2017). But around 1495, the inventor Leonardo da Vinci was already designing automatons and one of them was an anthropomorphic humanoid: the da Vinci's Knight shown in Figure 2.1. Although limited compared to today's robots, the knight was able to perform small programmable tasks and was advanced for its time (Moran, 2006). Over the years, the development of mathematical theories, the development of physics, and the emergence of electronics enabled the development of advanced humanoids: a product of private corporations and universities.

Figure 2.1: The da Vinci Knight.

In the academic world, the father of Japanese robotics,[1] Ichiro Kato, was responsible for the first humanoid robot design, developed during the Waseda Robot (WABOT) Project at Waseda University. Later, in 1984, the WL-10RD from the Waseda Legs (WL) series showed in Figure 2.2 (a), using the ZMP approach (Vukobratovic & Juricic, 1969), was the first humanoid to walk with a dynamically balanced gait (VUKOBRATOVIĆ & BOROVAC, 2004). In 1995, the Waseda Bipedal Humanoid (WABIAN) series, shown in Figure 2.2 (b), started being developed aiming to share information and behavioral spaces with humans (Hashimoto et al., 2002; Lim & Takanishi, 2007). From 1997 to 2009, Japan's Institute of Advanced Industrial Science and Technology (AIST) and Honda worked together in the development of the research humanoids Humanoid Research Project (HRP) series (Yokoi et al., 2004; Akachi et al., 2005; Hirukawa et al., 2004; Kajita et al., 2004; Kaneko et al., 2008; Kanehira et al., 2002).

In 2000, Nishiwaki from the University of Tokyo built the Humanoid 6 (H6) (Nishiwaki et al., 2000) and in 2006 the Humanoid 7 (H7) (Nishiwaki et al., 2007), showed in Figure 2.4, both humanoid platforms to test intelligent humanoid robotics and a follow-up of the child-size humanoid Humanoid 5 (H5), developed by the same group. In 2002, the Korean Advanced Institute of Science and Technology (KAIST) Humanoid Robot 1 (KHR-1), shown in Figure 2.5, was developed to realize a complete online motion control based on sensory feedback control (Kim et al., 2002; Kim & Oh, 2004). In 2005, the KAIST Humanoid Robot 2 (KHR-2) was released to be more robust, more human-friendly, compatible with many algorithms, and with a wider range of angular motion (Ill-Woo Park et al., 2005). Also in 2005, a humanoid design to be more human-like overall, the KAIST Humanoid Robot 3 (KHR-3) or HUBO, was developed. HUBO frequently participates in the Defence Advanced Research Projects Agency (DARPA) Robotics Challenge, and in 2015, it won the competition. In 2010, the small-size humanoid iCub, in Figure 2.6,

[1] https://www.waseda.jp/inst/fro/en/about/history/

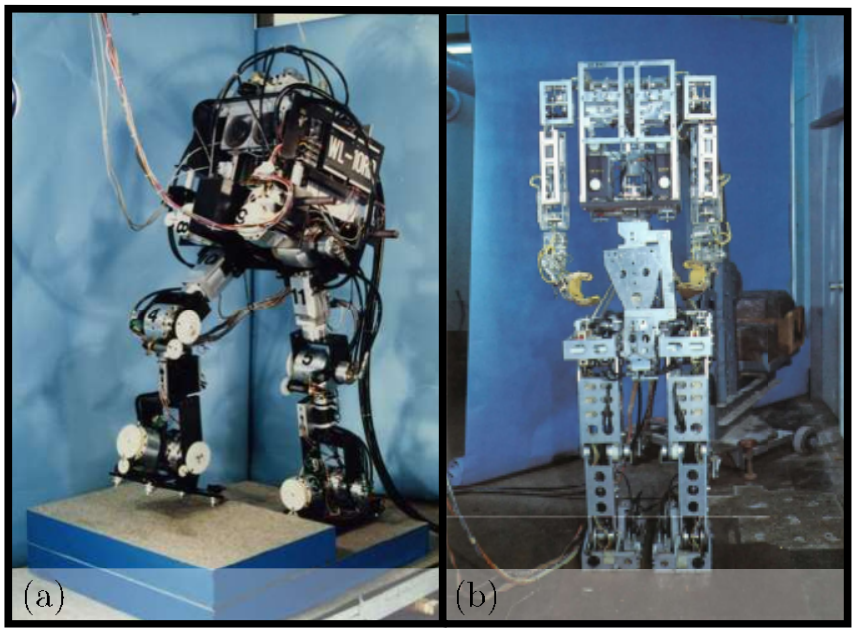

Figure 2.2: (a) WL-10DR was the first humanoid to perform a balanced walking; (b) WABOT-1.

Figure 2.3: Humanoid Robot Platform series.

was developed as a collaboration between several European universities to be a cognitive research platform (Metta et al., 2010).

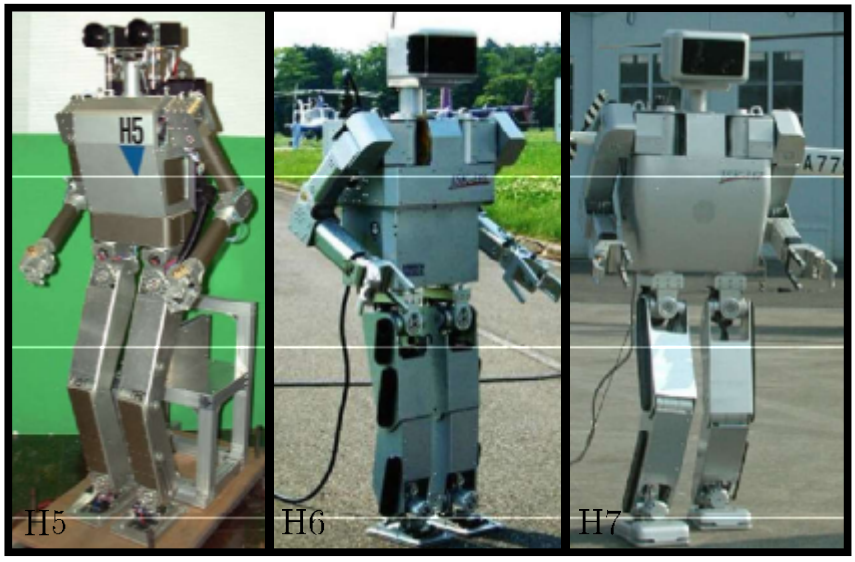

Figure 2.4: Humanoids H5, H6 and H7 from the Tokyo University.

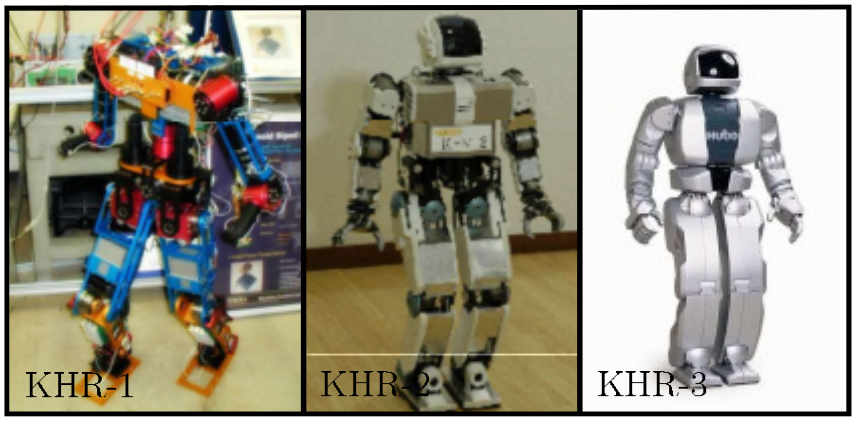

Figure 2.5: KAIST Humanoid Robot Series: KHR-1, KHR2, and KHR3 or HUBO.

Many technology companies around the world invested in developing humanoids. From 1986 to 1993, the Japanese Honda[2] developed the bipedal robots series E, in Figure 2.7 that has two legs, a platform containing controllers, anda power source. From 1993 to 1996, Honda presented the humanoid series P, in Figure 2.8, which has two legs, two arms, a head, a torso, and a backpack with the controller and power. The P series' initial goal was to collaborate with humans to perform tasks that we can't do (Hirai et al., 2007). In 2000, the ASIMO series, in Figure 2.9, was presented, a smaller and lighter robot that was developed to improve human life (Hirose & Ogawa, 2007). In 2011, the latest version of ASIMO had more features and was more adaptive to work with humans.[3] In

[2]https://global.honda/innovation/robotics/robot-development-history.html
[3]https://global.honda/innovation/robotics/ASIMO.html#2011

Figure 2.6: iCub Robot.

2003, Sony, another Japanese company, developed the Sony Dream Robot 3X (SDR-3X), in Figure 2.10, a humanoid walking and dancing prototype to be an intelligent home appliance (Christensen, 2003). In 2002, the more adaptive version, Sony Dream Robot 4X (SDR-4X), was launched (Fujita et al., 2003), and in 2003 the Sony Dream Robot 4XII (SDR-4XII), the first running humanoid (Akachi et al., 2005), was presented but it was not commercially available until 2018.[4] In 2008, Aldebaran Robots, now SoftBank Robotics of France, launched the NAO robot (Gouaillier et al., 2009), in Figure 2.11, a small humanoid famous for its synchronized dance at Universal Expo Shanghai in 2010 and its ability to play soccer. In 2009, Boston Dynamics presented a full-size humanoid Petman, in Figure 2.12, to test chemical-resistant military gear (Nelson et al., 2012). In 2011 the Korean Institute of Science and Technology presented Kibo, in Figure 2.13, a humanoid that can imitate human walking (Lee et al., 2015), and is made for human-robot interaction.[5]

The application of humanoids is further extended when considering how much these robots can help humans in places like outer space. In 2000, the National Aeronautics and Space Administration (NASA) started developing the Robonaut to help astronauts in missions (Ambrose et al., 2000; Bluethmann et al., 2003), but the first robot in space was the next version, the Robonaut 2 (Diftler et al., 2011). Both Robonauts did not walk. The first NASA walking humanoid was Valkyrie, in Figure 2.14, which was built to work in dangerous and inhospitable environments[6] (Radford et al., 2015).

Unfortunately, some robots are designed with a less noble goal in mind. In the last decade, we saw many military robots from the US military alongside Boston Dynamics. The most famous is the Bigdog[7], a quadruped robot that can carry heavy loads and keep

[4]https://www.sony.com/en/SonyInfo/CorporateInfo/History/sonyhistory-j.html
[5]http://www.robocare.co.kr/pages/product05_en.php
[6]https://www.nasa.gov/feature/r5/
[7]https://www.bostondynamics.com/legacy
https://www.darpa.mil/about-us/timeline/big-dog

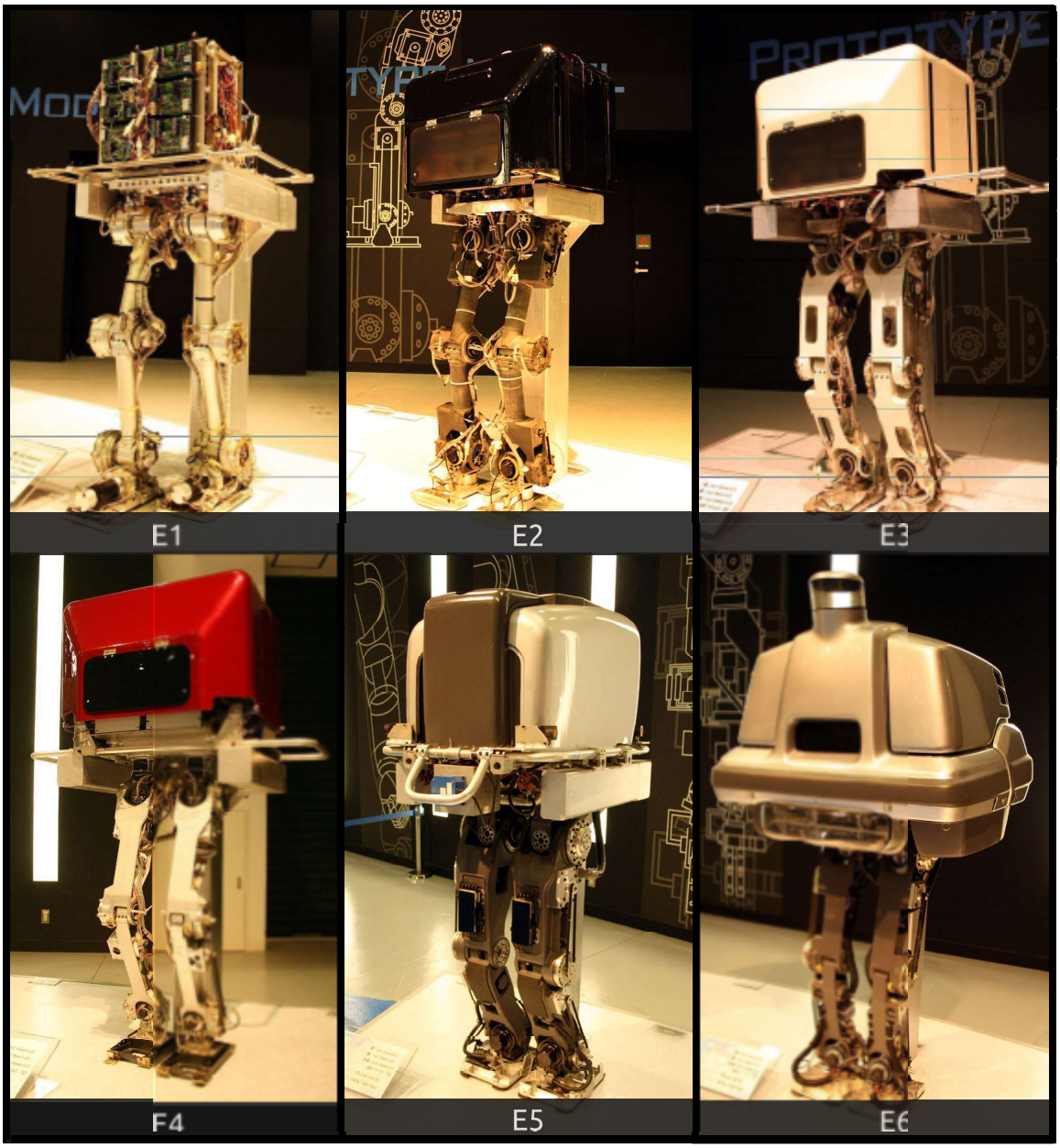

Figure 2.7: Honda E series: E1 to E6.

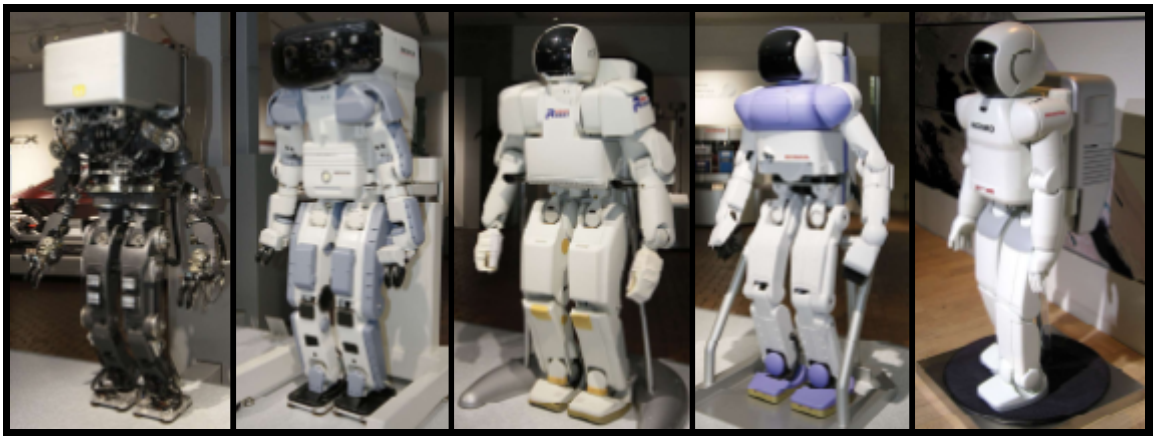

Figure 2.8: Honda P series: P1 to P4.

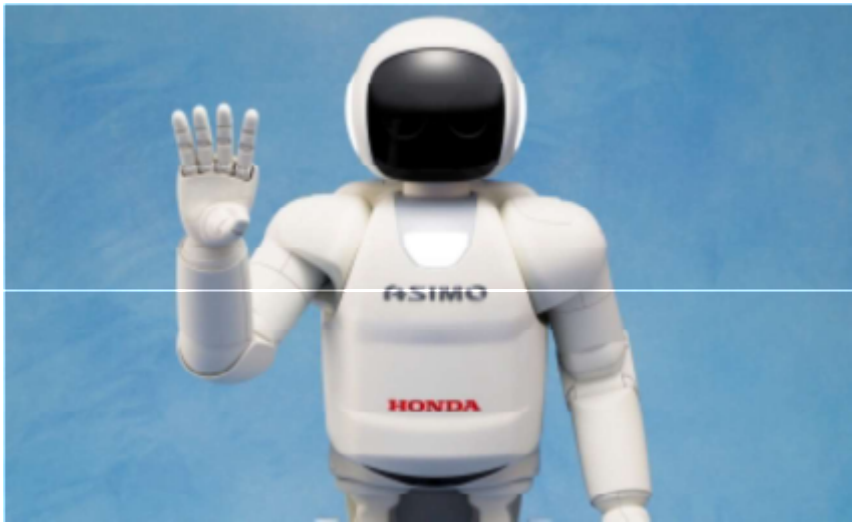

Figure 2.9: Honda ASIMO.

Figure 2.10: Sony Dream Robots: SDR-3X, SDR-4X, and SDR-4XII.

Figure 2.11: NAO Robot.

Figure 2.12: Boston Dynamics Petman Robot.

Figure 2.13: Kibo Robot.

Figure 2.14: Valkyrie Robot.

walking even when someone is kicking it. Boston Dynamic's humanoid counterpart is the Atlas, in Figure 2.15, which is increasing its functionality over the years: from walking in any terrain (Kuindersma et al., 2014, 2016; Wiedebach et al., 2016), to doing parkour and backflips[8]. Atlas is used for research, although the project was financed by DARPA.

Figure 2.15: Boston Dynamic Atlas Robot.

In 2012, an open-source low-budget child-size humanoid, Poppy, in Figure 2.16, was presented by the Flowers Laboratory[9] at the University of Bordeaux. The robot is a 3D printed humanoid available for anyone that can print and assemble it. Poppy has been used by our research group, MACRO, to test and simulate constrained controllers (Quiroz-Omana & Adorno, 2019; Urban & Adorno, 2019). In 2014, the German Aerospace

[8]https://www.youtube.com/watch?v=tF4DML7FIWk
[9]https://flowers.inria.fr/

Center developed the Torque-Controlled Humanoid Robot (TORO), in Figure 2.17, a torque-controlled humanoid platform to research bipedal walking and multi contacts, among other topics (Englsberger et al., 2014). Also in 2014, Romeo, in Figure 2.18, an assistive humanoid robot from the Romeo Project was shown as a prototype.[10] In 2015, Hanson Robotics released Sophia, the first robot to gain citizenship in the world. In 2017, when it became a citizen of Saudi Arabia, it could not walk, but since 2018, it gained legs and it could walk around.[11] Also in 2017, Toyota launched the Toyota Humanoid Robot 3 (T-HR3), in Figure 2.19, a humanoid that could mirror human actions. The 2020 version of the T-HR3 was aimed to help in the Olympic games.

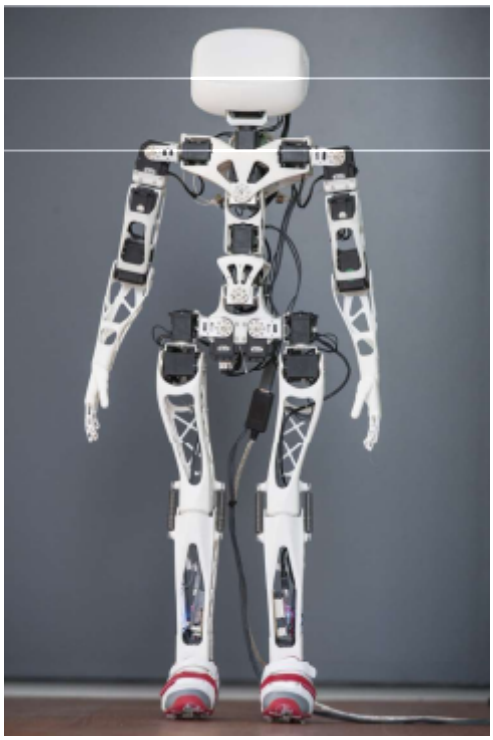

Figure 2.16: Poppy Humanoid Robot.

The next section presents the state of the art of techniques used to control some of the humanoids cited in this section. Some of them are based on the ZMP presented by Vukobratovic & Juricic (1969). A class of these models is the reduced-order model such as the spring-loaded inverted pendulum (SLIP)(Blickhan, 1989), the passive dynamic walking (McGeer, 1990a), and the hybrid zero dynamics (HZD) (Westervelt et al., 2018) are presented.

[10] https://projetromeo.wordpress.com/
[11] https://www.hansonrobotics.com/the-making-of-sophia-sophias-legs/

Figure 2.17: TORO Robot.

Figure 2.18: Romeo Robot.

Figure 2.19: Toyota Humanoid Robot: T-HR3.

2.2 Walking Controllers

Section. 2.1 presented a historical overview of the humanoid robots without describing the models and controllers used. This section, describes the most common models and controllers used for bipedal walking. The most important model for this work is the ZMP and the controllers based on it. For the sake of completeness, this section also briefly describe the reduced-order models, passive walking, and the hybrid zero dynamic (HZD).

2.2.1 ZMP-based controllers

Many works have addressed the walking challenge. Since the beginning of the 1970s, scientists have developed many methods that have improved over the years in complexity, efficiency, and functionality (Reher & Ames, 2021). Vukobratovic & Juricic (1969) were the first to simplify and describe the robot gait equations. They defined the ZMP, which is the point where all active forces can be reduced to a single resultant as well as the point where the horizontal components of the resultant moment are zero (Vukobratovic & Juricic, 1969; VUKOBRATOVIĆ & BOROVAC, 2004). From that work, (Kato et al., 1973) implemented the method in a real robot, WABOT-1. Many others have derived walking models based on the ZMP. Kajita & Tani (1991), for instance, simplified the walking model as an inverted pendulum. Later, Kajita et al. (2003) used a predictive control to calculate a trajectory for the ZMP. This technique controls the CoM using the ZMP equations. To introduce more adaptability to the ZMP controller, Kajita et al. (2006) proposed an auxiliary ZMP adding an inverse system to the generator pattern that changes the behavior of the robot during the walking cycle. This addition introduces errors in the ZMP that must be compensated by the virtual time-shifting of the ZMP reference. The main effect of this compensation was the adaptive change in the walking speed.

Although widely used, the Kajita et al. (2003) methodology is restricted regarding the

walking features such as where the feet starts, future steps, feet orientation, trajectory of the ZMP, and duration of the step. Some authors are more flexible with those features. Herdt et al. (2010), for instance, extended Kajita et al. (2003)'s work by modifying the predictive controller to automatically calculate the future footsteps and additionally impose constraints to guarantee feasibility and balance. Bohorquez & Wieber (2018) extended the work of Herdt et al. (2010) to allow the robot to adapt its foot orientation to walk in a crowd, avoiding any collisions. Naveau et al. (2017) imposed balance and step orientation constraints, and obstacle-avoidance constraints using a non-linear predictive controller. To handle contact constraints such as friction and contact forces, Kuindersma et al. (2014) proposed a controller based on quadratic programming that guarantees a dynamically stable walk while minimizing joints acceleration, ensuring that the dynamics and input limits are respected, and that contact forces remain within a threshold. Feng et al. (2015) proposed a two-level minimization controller: a high-level controller to produce the CoM and swing foot trajectories and constrain the center of pressure, friction, and joint limits; and a low-level whole-body controller to track the high-level trajectories. Examples of robots whose gait is based on the ZMP are the ASIMO from Honda (Hirose & Ogawa, 2007), the Sony HRP robot series (Hirukawa et al., 2004; Akachi et al., 2005; Kaneko et al., 2008; Kanehira et al., 2002; Yokoi et al., 2004), and the HUBO robot from KAIST (Ill-Woo Park et al., 2005).

Although our method is based on the ZMP, we do not use predictive controllers as (Kajita et al., 2003). Also, our ZMP trajectory is more flexible since we can produce a more or less conservative trajectory, depending on the set of constraints we choose.

2.2.2 Reduced-order models based controllers

In the 1980s, ZMP-based walking strategies were a limitation to the humanoid walking field. The developed methods were conservative and did not exploit entirely the intrinsic dynamic non-linearities of the robots. To develop stable and efficient methods, at the MIT, Raibert (1984, 1986) explored underactuated robots, experimenting with hopping robots that were able to run and flip (Reher & Ames, 2021). The hopping robots model used in Raibert's research was a reduced-order model.

Reduced-order models are advantageous due to their efficiency and robustness (Reher & Ames, 2021). These models enable a stable cyclic movement by considering the entire robot mass in the hips and the robot legs as components such as springs and dampers. The spring-loaded inverted pendulum (SLIP) is a set of models which reduces the system's order. The SLIP-based controller has three control objectives: regulate foot position, regulate CoM height, and regulate robot posture which produces reaction forces with a characteristic double hump. The double hump is desirable due to its similarities to those shown in biological gaits (Schwind & Koditschek, 2000; Reher & Ames, 2021). Examples of

robots modeled with SLIP are the Compliant Humanoid Platform (COMAN) (Kormushev et al., 2011) and the NASA's Valkyrie (Radford et al., 2015). One of the advantages of this strategy besides the lower order is the ability to surpass small disturbances. To understand the appeal of such a set of reduced-order models, it is useful to think of biological structures (Schwind & Koditschek, 2000).

Observing the biological locomotion structures of animals, the muscle-skeletal system can be simplified to several non-linear actuated spring-mass systems. This analogy was exploited and further simplified by Blickhan (1989), who proposed the spring-mass model for running and hopping robots. Later, Geyer et al. (2006) extended the method to unify the walking and running models.

Another reduced-order strategy was proposed by Pratt et al. (2001) to model the robot using virtual components (springs, dampers, masses, and non-linear potential fields, for instance), which produce desired forces and torques when the robot interacts with the environment. If the goal is, for instance, to smothly place the hand of the robot on the table, we can add a spring and a damper in the model, so the behavior will change according to the virtual components attached to the robot. The virtual model control was implemented in Spring Flamingo (Hunter et al., 1991) and the Spring Turkey (Hunter et al., 1991).

2.2.3 Hybrid Models based controllers

Here we will present the two main groups of hybrid walking models and the respective control techniques: the Passive Dynamic and the HZD. A hybrid model is divided into two phases (Grizzle et al., 2001): a continuous phase where the robot swings one of the legs forward and a discrete phase characterized by an impact of the swinging foot to the floor and by the support leg change.

2.2.3.1 Passive Dynamic

Passive walking can be described as a non-actuated gait. A planar non-actuated robot is placed in an initial position on the top of a downhill, for instance, and released. The result will be a robot descending a slope without any actuation. This kind of walking takes advantage of the gravity to perform a descendant trajectory given the initial set of conditions (McGeer et al., 1990). This set of robots was modeled as a hybrid model with the aforementioned continuous and discrete phases.

The dynamic passive walking was introduced by Ted McGeer's work (McGeer, 1988, 1990b,a, 1993). He explored passive robots by proposing a passive dynamic walking that although less conservative had problems performing in the presence of disturbances (Reher & Ames, 2021). Another problem with these passive models was the lack of a formal approach to deal with the non-linearities of the system.

Some works introduced a level of actuation to perform the passive walking and compensate the gravity and external disturbances, such as the Cornell Walkers and the MIT learning bipedals (Reher & Ames, 2021). Adding actuators to those passive robots (Tedrake et al., 2004; Anderson et al., 2005) opened the possibility of exploring the concept of controlled symmetries (Spong & Bullo, 2005), which also expanded the technique to 3D robots.

2.2.3.2 Hybrid Zero Dynamic

In order to prove close-loop asymptotic stability, Grizzle et al. (2001), used the hybrid model with feedback controllers. A non-linear controller, to address the hybrid model and non-linearities of the walking nature, were first proposed by Grizzle et al. (2001); Westervelt et al. (2003).

The hybrid model was the same as the passive dynamic model. However, virtual constraints (Westervelt et al., 2018) and a zero dynamic surface (Reher & Ames, 2021) were added to control the movement of all limbs. The virtual constraints are a set of functions used in non-linear controllers added to synchronize the robot limbs movement towards a desired behavior (Westervelt et al., 2018). They are called virtual because they are added via controller. The feedback linearization controller was derived based on the hybrid model and based on the virtual constraints (Westervelt et al., 2018). The HZD is the result of zeroing a set of virtual constraints. The zero dynamics surface is characterized by the cancellation of the system dynamics in closed loop which can be modulated to achieve stability (Reher & Ames, 2021).

The HZD, first, imposes a hybrid invariance, i.e., the impacts are ignored and an invariant attractive surface is design so the controller will evolve inside this surface. But since the impacts are not neglectable due to an instant change of velocity, a constraint is imposed during the impact to provide impact invariance to the surface (Westervelt et al., 2018).

The advantage of hybrid models is that we can work with the dynamics of the robot and perform faster tasks. However, the concepts and the implementation are more complex than the methods based on the ZMP, since they use non-linear models and controllers, and take into consideration impacts effects.

2.3 Chapter summary

This chapter has presented a brief history of humanoids in Section. 2.1, and the main models and controller techniques in Sec. 2.2. Section. 2.1 has showed some famous robots from the academy such as IIUBO (Ill-Woo Park et al., 2005) and the industry such as NAO (Gouaillier et al., 2009).

Section 2.2 has presented the concepts of the ZMP-based controllers, the reduced-order controllers, and the hybrid models based controllers.

3 Mathematical Background

Our method uses dual quaternion algebra, which offers several advantages over other mathematical frameworks (Adorno, 2017). Since dual quaternions are used to represent rigid motions and geometrical primitives such as Plücker lines, planes, and cylinders, we take advantage of dual quaternion algebra during robot modeling and control, as well as to impose the constraints related to the biped walking task since it simplifies the representation of the primitives and the calculation of the distance Jacobians between such primitives. As a result, we obtain a straightforward and compact framework for the quasi-static biped walking task.

3.1 Quaternions and Dual Quaternions

Hamilton introduced the quaternions in the nineteenth century as an extension of the complex numbers (Adorno, 2011). The set of quaternions is defined as

$$\mathbb{H} \triangleq \left\{ h_1 + h_2\hat{\imath} + h_3\hat{\jmath} + h_4\hat{k} : h_1, h_2, h_3, h_4 \in \mathbb{R} \right\},$$

where $\hat{\imath}$, $\hat{\jmath}$, and $\hat{k}$ are imaginary units such that

$$\hat{\imath}^2 = \hat{\jmath}^2 = \hat{k}^2 = \hat{\imath}\hat{\jmath}\hat{k} = -1.$$

The quaternions can perform mathematical operations such as addition, multiplication, norm, cross product, and dot product, as shown in (Adorno, 2017). They also represent

translations and rotations in $\mathbb{R}^3$. Given a quaternion $\boldsymbol{h} = h_1 + h_2\hat{\imath} + h_3\hat{\jmath} + h_4\hat{k}$, we define $\mathrm{Re}\,(\boldsymbol{h}) \triangleq h_1$ as the real part, $\mathrm{Im}\,(\boldsymbol{h}) \triangleq h_2\hat{\imath} + h_3\hat{\jmath} + h_4\hat{k}$ as the imaginary part, and $\boldsymbol{h}^* \triangleq \mathrm{Re}\,(\boldsymbol{h}) - \mathrm{Im}\,(\boldsymbol{h})$ as the conjugate. Positions and translations are given by pure quaternions, which are defined as a quaternion with real part equal to zero. Thus, a position is given by

$$\boldsymbol{p} = p_1\hat{\imath} + p_2\hat{\jmath} + p_3\hat{k},$$

where p_1, p_2, and p_3 are, respectively, the x, y, and z coordinates. A translation transformation from $\mathcal{F}_0$ to $\mathcal{F}_1$ of p_t units in the y-axis, for instance, is given by $\boldsymbol{p}_1^0 = p_t\hat{\jmath}$. In Fig. 3.1, we see the representation of the point $\boldsymbol{p}$ in $\mathcal{F}_0$ in A and the translation $\boldsymbol{p}_1^0$ in B.

The rotation is a unit quaternion, which is a quaternion that satisfy $\boldsymbol{h}^*\boldsymbol{h} = 1$, is given by

$$\boldsymbol{r} = \cos\frac{\phi}{2} + \boldsymbol{n}\sin\frac{\phi}{2},$$

where ϕ is the rotation angle and $\boldsymbol{n}$ is a pure unit norm quaternion representing the rotation axis. For instance, in Fig. 3.1 shows the rotation of $-\phi_z$ in the z axis, $\boldsymbol{r}_2^1 = \cos\left(-\frac{\phi_z}{2}\right) + \hat{k}\sin\left(-\frac{\phi_z}{2}\right)$.

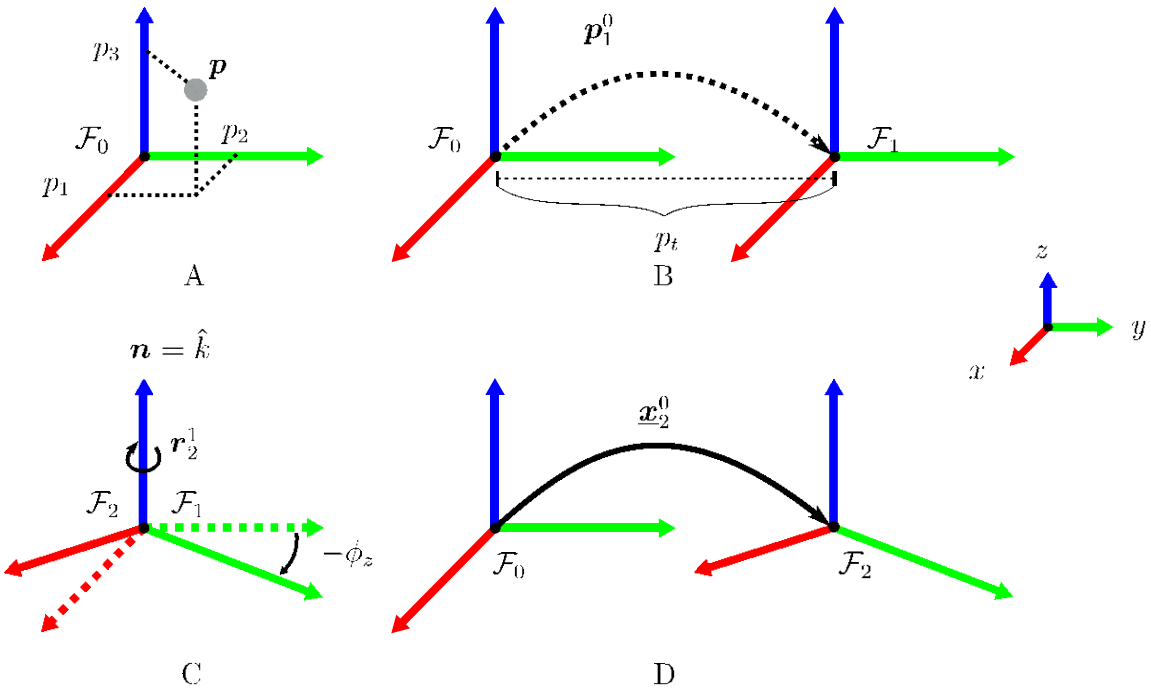

Figure 3.1: Quaternions and dual quaternions representation: A. Point in coordinates (p_1, p_2, p_3); B. Transformation from $\mathcal{F}_0$ to $\mathcal{F}_1$: a translation of p_t along the y-axis given by $\boldsymbol{p}_1^0 = p_t\hat{\jmath}$; C. Transformation from $\mathcal{F}_1$ to $\mathcal{F}_2$: a rotation of $-\phi$ around the z-axis; and D. A rigid transformation from $\mathcal{F}_0$ to $\mathcal{F}_2$: a translation of p_t along the y-axis followed by a rotation of ϕ around the z-axis.

Also in the nineteenth century, Clifford introduced the dual number set (Adorno, 2011).

The dual number is formed by two parts: the primary part and the secondary part. The primary part is a real number, and the dual part is a real number multiplied by the dual unit ε. The dual unit has the following properties:

$$\varepsilon \neq 0$$
$$\varepsilon^2 = 0.$$

The dual quaternion is an extension of the dual number of Clifford and the set is defined as

$$\mathcal{H} \triangleq \left\{ \boldsymbol{h} + \varepsilon \boldsymbol{h}' : \boldsymbol{h}, \boldsymbol{h}' \in \mathbb{H}, \varepsilon^2 = 0, \varepsilon \neq 0 \right\}.$$

Given a dual quaternion $\underline{\boldsymbol{h}} = h_1 + h_2\hat{\imath} + h_3\hat{\jmath} + h_4\hat{k} + \varepsilon\left(h_1' + h_2'\hat{\imath} + h_3'\hat{\jmath} + h_4'\hat{k}\right)$, we define the real part as $\mathrm{Re}\left(\underline{\boldsymbol{h}}\right) \triangleq h_1 + \varepsilon h_1'$, the imaginary part as $\mathrm{Im}\left(\underline{\boldsymbol{h}}\right) \triangleq h_2\hat{\imath} + h_3\hat{\jmath} + h_4\hat{k} + \varepsilon\left(h_2'\hat{\imath} + h_3'\hat{\jmath} + h_4'\hat{k}\right)$, and the conjugate as $\underline{\boldsymbol{h}}^* \triangleq \mathrm{Re}\left(\underline{\boldsymbol{h}}\right) - \mathrm{Im}\left(\underline{\boldsymbol{h}}\right)$. Dual quaternions with unit norm, called unit dual quaternions, satisfy $\underline{\boldsymbol{h}}\underline{\boldsymbol{h}}^* = \underline{\boldsymbol{h}}^*\underline{\boldsymbol{h}} = 1$ and represent rigid motions composed of rotation and translation. The pose is given by

$$\underline{\boldsymbol{x}} = \boldsymbol{r} + \varepsilon\frac{1}{2}\boldsymbol{p}\boldsymbol{r}. \tag{3.1}$$

A sequence of rigid motions is given by a sequence of dual quaternion multiplications. For instance, consider the unit dual quaternions $\underline{\boldsymbol{x}}_1^0$ and $\underline{\boldsymbol{x}}_2^1$ that represent the rigid motions (translation plus rotation) from frame $\mathcal{F}_0$ to frame $\mathcal{F}_1$ and from $\mathcal{F}_1$ to $\mathcal{F}_2$, respectively. The rigid motion from $\mathcal{F}_0$ to $\mathcal{F}_2$ is given by $\underline{\boldsymbol{x}}_2^0 = \underline{\boldsymbol{x}}_1^0\underline{\boldsymbol{x}}_2^1$. In Fig. 3.1 D, we see a pure translation, $\underline{\boldsymbol{x}}_1^0 = 1 + \varepsilon\frac{1}{2}\boldsymbol{p}_1^0$, followed by a pure rotation, $\underline{\boldsymbol{x}}_2^1 = \boldsymbol{r}_2^1$.

Given two pure quaternions $\boldsymbol{a}$ and $\boldsymbol{b}$, the inner product $\langle \boldsymbol{a}, \boldsymbol{b} \rangle \triangleq -\left(\boldsymbol{a}\boldsymbol{b} + \boldsymbol{b}\boldsymbol{a}\right)/2$ and the cross product $\boldsymbol{a} \times \boldsymbol{b} \triangleq \left(\boldsymbol{a}\boldsymbol{b} - \boldsymbol{b}\boldsymbol{a}\right)/2$ have the same geometrical interpretation of the inner and cross products of vectors in $\mathbb{R}^3$. Also, the pure quaternion $\boldsymbol{h} = h_2\hat{\imath} + h_3\hat{\jmath} + h_4\hat{k}$ can be mapped to $\mathbb{R}^3$ as $\mathrm{vec}_3\,\boldsymbol{h} = \begin{bmatrix} h_2 & h_3 & h_4 \end{bmatrix}^T$, and the dual quaternion $\underline{\boldsymbol{h}}$ can be mapped to $\mathbb{R}^8$ as $\mathrm{vec}_8\,\underline{\boldsymbol{h}} = \begin{bmatrix} h_1 & h_2 & h_3 & h_4 & h_1' & h_2' & h_3' & h_4' \end{bmatrix}^T$.

Given two pure quaternions $\boldsymbol{a}$ and $\boldsymbol{b}$, the Hamilton operators satisfy the equalities $\mathrm{vec}_4\left(\boldsymbol{a}\boldsymbol{b}\right) = \overset{+}{\boldsymbol{H}}_4\left(\boldsymbol{a}\right)\mathrm{vec}_4\left(\boldsymbol{b}\right) = \overset{-}{\boldsymbol{H}}_4\left(\boldsymbol{b}\right)\mathrm{vec}_4\left(\boldsymbol{a}\right)$, where $\overset{+}{\boldsymbol{H}}_4\left(\cdot\right)$ and $\overset{-}{\boldsymbol{H}}_4\left(\cdot\right)$ are the Hamilton operators defined as (Adorno, 2017)

$$\overset{+}{\boldsymbol{H}}_4\left(\boldsymbol{h}\right) \triangleq \begin{bmatrix} h_1 & -h_2 & -h_3 & -h_4 \\ h_2 & h_1 & -h_4 & h_3 \\ h_3 & h_4 & h_1 & -h_2 \\ h_4 & -h_3 & h_2 & h_1 \end{bmatrix}, \quad \overset{-}{\boldsymbol{H}}_4\left(\boldsymbol{h}\right) \triangleq \begin{bmatrix} h_1 & -h_2 & -h_3 & -h_4 \\ h_2 & h_1 & h_4 & -h_3 \\ h_3 & -h_4 & h_1 & h_2 \\ h_4 & h_3 & -h_2 & h_1 \end{bmatrix}. \tag{3.2}$$

Given two dual quaternions $\underline{\boldsymbol{x}}$ and $\underline{\boldsymbol{y}}$, we can use the Hamilton operators such that

$$\operatorname{vec}_8\left(\underline{\boldsymbol{x}}\underline{\boldsymbol{y}}\right) = \overset{+}{\boldsymbol{H}}_8\left(\underline{\boldsymbol{x}}\right)\operatorname{vec}_8\underline{\boldsymbol{y}} = \overset{-}{\boldsymbol{H}}_8\left(\underline{\boldsymbol{y}}\right)\operatorname{vec}_8\left(\underline{\boldsymbol{x}}\right),$$

where

$$\overset{+}{\boldsymbol{H}}_8\left(\underline{\boldsymbol{h}}\right) \triangleq \begin{bmatrix} \overset{+}{\boldsymbol{H}}_4\left(\boldsymbol{h}_{\mathcal{P}}\right) & \boldsymbol{0}_{4\times4} \\ \overset{+}{\boldsymbol{H}}_4\left(\boldsymbol{h}_{\mathcal{D}}\right) & \overset{+}{\boldsymbol{H}}_4\left(\boldsymbol{h}_{\mathcal{P}}\right) \end{bmatrix}, \quad \overset{-}{\boldsymbol{H}}_8\left(\underline{\boldsymbol{h}}\right) \triangleq \begin{bmatrix} \overset{-}{\boldsymbol{H}}_4\left(\boldsymbol{h}_{\mathcal{P}}\right) & \boldsymbol{0}_{4\times4} \\ \overset{-}{\boldsymbol{H}}_4\left(\boldsymbol{h}_{\mathcal{D}}\right) & \overset{-}{\boldsymbol{H}}_4\left(\boldsymbol{h}_{\mathcal{P}}\right) \end{bmatrix}. \tag{3.3}$$

3.2 Differential Kinematics

Consider a serial kinematic chain, whose end-effector pose, $\underline{\boldsymbol{x}} \triangleq \underline{\boldsymbol{h}}(\boldsymbol{q})$, is given by a unit dual quaternion as in (3.1). The differential forward kinematics (DFK) maps the joints velocities to the end-effector (generalized) velocities, which is given by

$$\operatorname{vec}_8\dot{\underline{\boldsymbol{x}}} = \boldsymbol{J}\left(\boldsymbol{q}\right)\dot{\boldsymbol{q}},$$

where $\boldsymbol{J}\left(\boldsymbol{q}\right) \in \mathbb{R}^{8\times n}$ is the Jacobian matrix and $\boldsymbol{q} \in \mathbb{R}^n$ is the vector of robot configurations. From the DFK and (3.1), it is possible to find the Jacobians that satisfy $\operatorname{vec}_3\dot{\boldsymbol{p}} = \boldsymbol{J}_p\dot{\boldsymbol{q}}$ and $\operatorname{vec}_4\dot{\boldsymbol{r}} = \boldsymbol{J}_r\dot{\boldsymbol{q}}$ (Adorno et al., 2010).

3.3 Geometric Primitives

We can use dual quaternions to represent geometric primitives such as Plücker lines, cylinders and planes.

3.3.1 Cylinders

An infinite cylinder is defined as the pair $(\underline{\boldsymbol{l}}, r)$, where $\underline{\boldsymbol{l}} = \boldsymbol{l} + \varepsilon\left(\boldsymbol{p}\times\boldsymbol{l}\right)$ is a dual quaternion that represents its centerline, a Plücker line, and r represents its radius. Furthermore, $\boldsymbol{l}$ is a pure quaternion with unit norm that represents the line direction, and $\boldsymbol{p}$ is pure quaternion that represents an arbitrary point on the line, as shown in Fig. 3.2 (Adorno, 2017).

3.3.2 Planes

A plane $\underline{\boldsymbol{\pi}}$ is described by the dual quaternion $\underline{\boldsymbol{\pi}} = \boldsymbol{n} + \epsilon d$, where $\boldsymbol{n}$ is a pure quaternion with unit norm that represents the normal to the plane, $d = \langle \boldsymbol{p}, \boldsymbol{n}\rangle$ is the perpendicular distance from the origin of the reference frame, and $\boldsymbol{p}$ is a pure quaternion that represents an arbitrary point on the plane, as shown in Fig. 3.3 (Adorno, 2017).

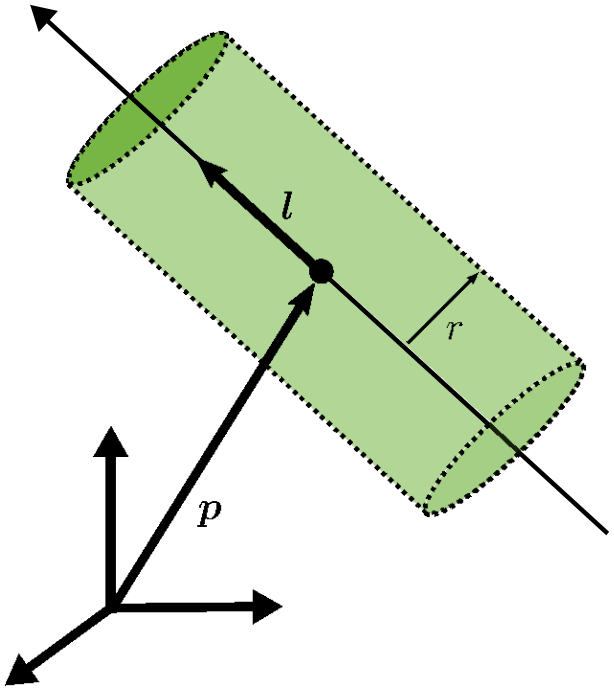

Figure 3.2: Cylinder with centerline $\underline{\boldsymbol{l}}$ and radius r. The line direction is denoted by $\boldsymbol{l}$ and, $\boldsymbol{p}$ is an arbitrary point on the line.

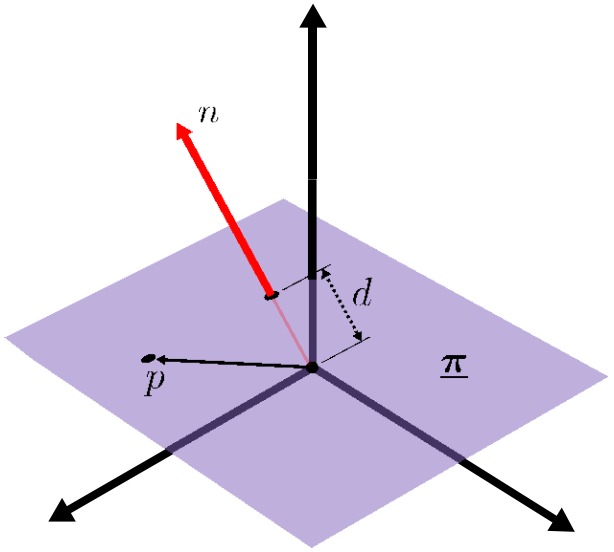

Figure 3.3: Plane $\underline{\boldsymbol{\pi}}$ with normal $\boldsymbol{n}$ and distance d.

3.4 Chapter summary

This chapter has showed the algebra used to model, control, and impose the constraints on our robot. We also present the differential kinematic model using this algebra. These concepts are used in Chapter 4 to produce the robot kinematic model and in Chapter 5 to derive the primitives used to impose the constraints on the controller.

4

Bipedal Walking Modeling

This section details the modeling of the walking based on Kajita et al. (2003)'s method, the ZMP, and the cart-table model. We explain how the ZMP relates to the CoM and the CoP and also a brief explanation of what happens to the ZMP when the robot support polygon collapses to a line in the border of the foot, what Vukobratović et al. (2006) calls the fictitious ZMP.

4.1 Bipedal Walking

The bipedal walking is divided into two phases: the single support phase (SSP) and the double support phase (DSP), which are alternated during the walking cycle and represent a change in the SP model and control dynamics. Figure 4.1 shows the complete walking cycle and how the phases alternate. The walking cycle is divided into four phases, as shown in Figure 4.1. In A) the robot is in its initial configuration and the first DSP occurs. The red cross shows that the CoM projection starts outside the left foot convex hull, the green cross is the desired CoM projection at the end of the DSP, and the blue arrow shows this transference. In B) occurs the first SSP, where the right foot swings from the back to the front, as shown by the pink arrow. The green cross represents the CoM inside the allowable region, the blue arrow shows the next DSP transference. In C) we have the second SSP, where the left foot swings from the back to the front towards the desired pose as shown by the pink arrow, while the CoM is inside the convex hull of the right foot as shown by the green cross, the blue arrow shows the next DSP and in D) the cycle starts

again from the configuration shown in B.

In the quasi-static bipedal walking, we assume low velocities and small accelerations, which implies from the equations of (Kajita et al., 2003) that the ZMP can be approximated by the CoM projection onto the ground. The ZMP is detailed in Section 4.2, and the quasi-static gait is shown in Section 4.4.

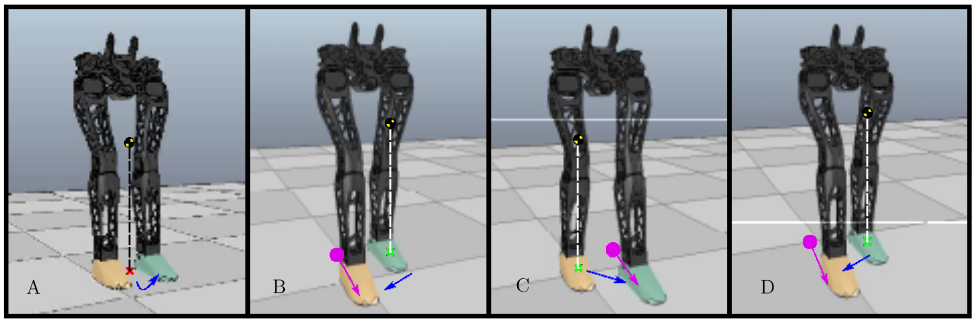

Figure 4.1: Walking phases: A) initial robot configuration and the first DSP. The *red* cross shows that the CoM projection starts outside the left foot convex hull, the *green* cross is the desired CoM projection at the end of the DSP, and the *blue* arrow shows this transference; B) the first SSP, where the right foot swings from the back to the front, as shown by the *pink* arrow. The *green* cross represents the CoM inside the allowable region, the blue arrow shows the next DSP transference; C) the second SSP, where the left foot swings from the back to the front towards the desired pose as shown by the pink arrow, while the CoM is inside the convex hull of the right foot as shown by the green cross, the blue arrow shows the next DSP; and in D the cycle starts again from the configuration shown in B.

4.2 The Zero Moment Point

The ZMP is the point where all active forces can be reduced to a single resultant as well as the point where the horizontal components of the resultant moment are zero (Vukobratovic & Juricic, 1969; VUKOBRATOVIĆ & BOROVAC, 2004). We calculate the ZMP by considering all the forces and momentum acting on the support foot. Since we choose to implement a quasi-static gait both the ZMP and the CoM projection are the same. We further explain this in Section 4.4.

Another important concept related to bipedal walking that can be confused with the ZMP is the concept of center of pressure (CoP). Although one might think the ZMP and the CoP are always the same, they are generally different. We show this difference in the next section.

4.3 Center of Pressure and Fictitious ZMP

In the literature, there are several misunderstands regarding the ZMP and the center of pressure CoP. According to VUKOBRATOVIĆ & BOROVAC (2004), the force acting at the CoP replaces the pressure between the foot and the ground. The ZMP and the CoP are coincident when this force acting on the CoP balances all active forces acting on the mechanism during the motion. However, when this balance is not achieved, the ZMP does not exist. The mechanism starts collapsing and the CoP is somewhere in the contact surface between the foot and the floor.

In Figure 4.2, from VUKOBRATOVIĆ & BOROVAC (2004), we can see the relation between the ZMP and the CoP depending on the mechanism's dynamic behavior. We can see, represented by the yellow arrows, the reaction force f_r and by the curved arrow the momentum τ. In Figure 4.2 (a), the ZMP coincides with the CoP, and the robot is in stable balance; in Figure 4.2 (b), a disturbance makes the foot start rolling over one border, while the CoP remains inside the support polygon defined by a strip, while the fictitious ZMP distance from the foot edge represents the intensity of the perturbation moment. Finally, in Figure 4.2 (c), we have a special case where the ZMP and the CoP are inside the support polygon, which collapses into a single strip and the robot is in an unstable balance. Thus, when the robot is somehow in a dynamic balance, the ZMP and the CoP exist and they are the same.

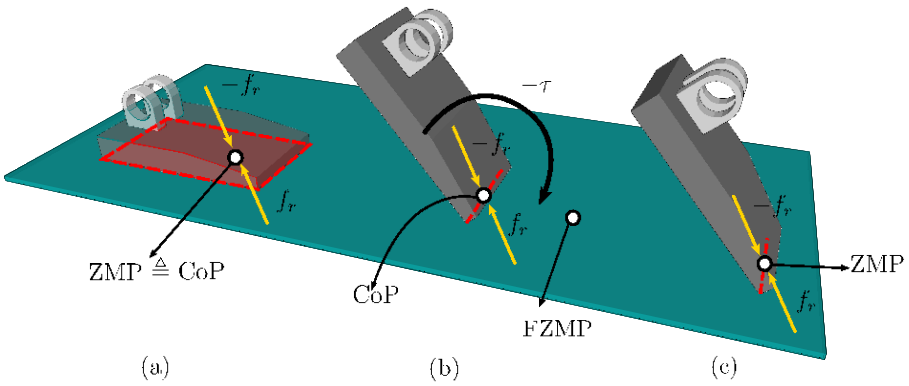

Figure 4.2: Relationship between the ZMP and the CoP.

We called the point represented in Figure 4.2(b) the fictitious ZMP (FZMP). According to VUKOBRATOVIĆ & BOROVAC (2004), when the robot is under a disturbance and the mechanism starts to roll over one foot's border, immediately, the ZMP will be moved away from the SP and it will be called the fictitious ZMP. During this phenomenon, the ZMP and the CoP do not coincide.

4.4 The Cart-Table model

Besides the CoP and the ZMP relation, we also have a relation between the ZMP and the CoM. The relationship between the CoM and the ZMP used in this thesis is derived from the cart-table model (Kajita et al., 2003), which is a simplification for the dynamics of the robot. The model consists of a massless table that has a single leg with a pin point foot in the geometric center of the tabletop, as shown in Figure 4.3, and a cart with mass m on the tabletop. The model follows the Three-Dimensional Linear Inverted Pendulum Model proposed by Kajita et al. (2003). When the car moves toward one of the borders, the table bends in the same direction, so the cart's ZMP is inside the pinpoint foot contact area with the floor. This guarantees the entire structure balance according to the dynamic condition for stability stated by Vukobratovic & Juricic (1969). However, this balance will not be achieved depending on the cart's acceleration rate.

The cart movement is limited to the tabletop, a plane, and if we consider the plane is horizontal, the relationship between the ZMP and the CoM of the cart is given by

$$\ddot{y}_c = -\frac{g}{z_c}\left(y_c - p_y\right), \tag{4.1}$$

$$\ddot{x}_c = -\frac{g}{z_c}\left(x_c - p_x\right), \tag{4.2}$$

where (p_x, p_y) is the location of the ZMP on the floor, (x_c, y_c) is the location of the cart CoM in the table, g is the gravitational acceleration, and z_c is the distance between the tabletop and the floor. Equations (4.1) and (4.2) are called the ZMP equations and are derived by Kajita et al. (2003).

Additionally, since we consider a quasi-static gait, the accelerations can be neglected. Thus, we can further simplify Equations 4.1 and 4.2 as

$$y_c = p_y,$$

$$x_c = p_x,$$

and use the kinematic model shown in Section 4.8 to model the robot. As we show in Chapter 5, we use the kinematic model to control the robot in SSP and the CoM to control the robot in DSP.

This cart-table model is important because it is used during the entire walking cycle. The support phases of the cycle are presented in Sections 4.5 and 4.6.

4.5 Double Support Phase

The DSP is the starting phase, where the robot has both feet in contact with the floor and the CoM projection is transferred to the new support foot. Fig 4.4 shows both feet

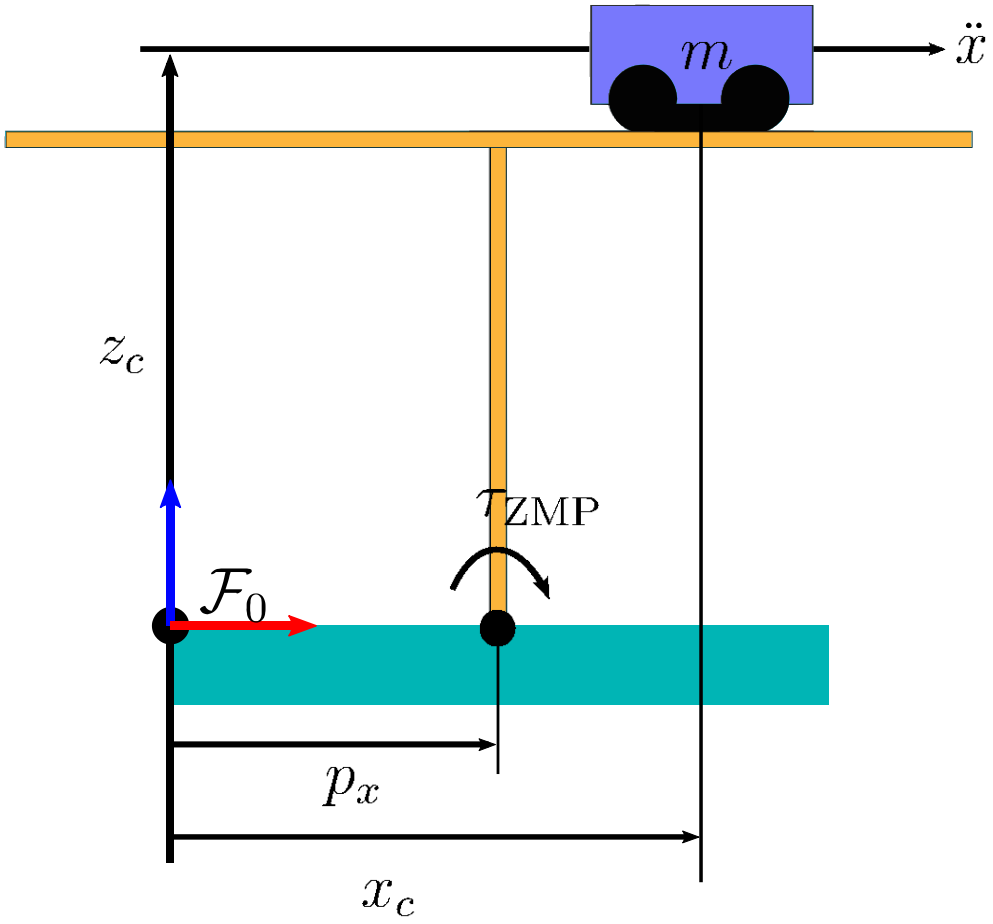

Figure 4.3: Planar representation of the cart-table model: the cart with mass m on the table; the inertial coordinate system as $\mathcal{F}_0$; the location of the ZMP, p_x; the location of the cart CoM on the table, x_c; and the momentum around the ZMP point, τ_{ZMP}.

area in *gray* and the convex hull in *light green*, which are combined into the SP during the DSP, as shown by the area delimited by the red line. The SP can be modeled by as many planes as necessary to represent it faithfully. However, we simplify it by selecting two planes: the tip plane $\underline{\boldsymbol{\pi}}_{\text{tip}}$ and the back plane $\underline{\boldsymbol{\pi}}_{\text{back}}$. The two additional planes in the outer borders that would be needed to complete the rectangle enclosing the feet are not necessary because the constrained motion controller, described in Chapter 5, ensures closed-loop stability. Therefore, when the CoM projection is transferred from one foot to the other, it never goes toward the outer border of the first foot. Moreover, as we enforce a first-order closed-loop error dynamics, there is no overshoot, hence the CoM projection does not reach the outer border of the second foot either.

A plane $\underline{\boldsymbol{\pi}}$ is completely represented, within dual quaternion algebra, by its normal $\boldsymbol{n}$ and its distance d to a reference frame such that $\underline{\boldsymbol{\pi}} = \boldsymbol{n} + \epsilon d$ (Adorno, 2017).

After the DSP, the next support phase is the SSP, whose definition and related constraints are shown in Section 4.6.

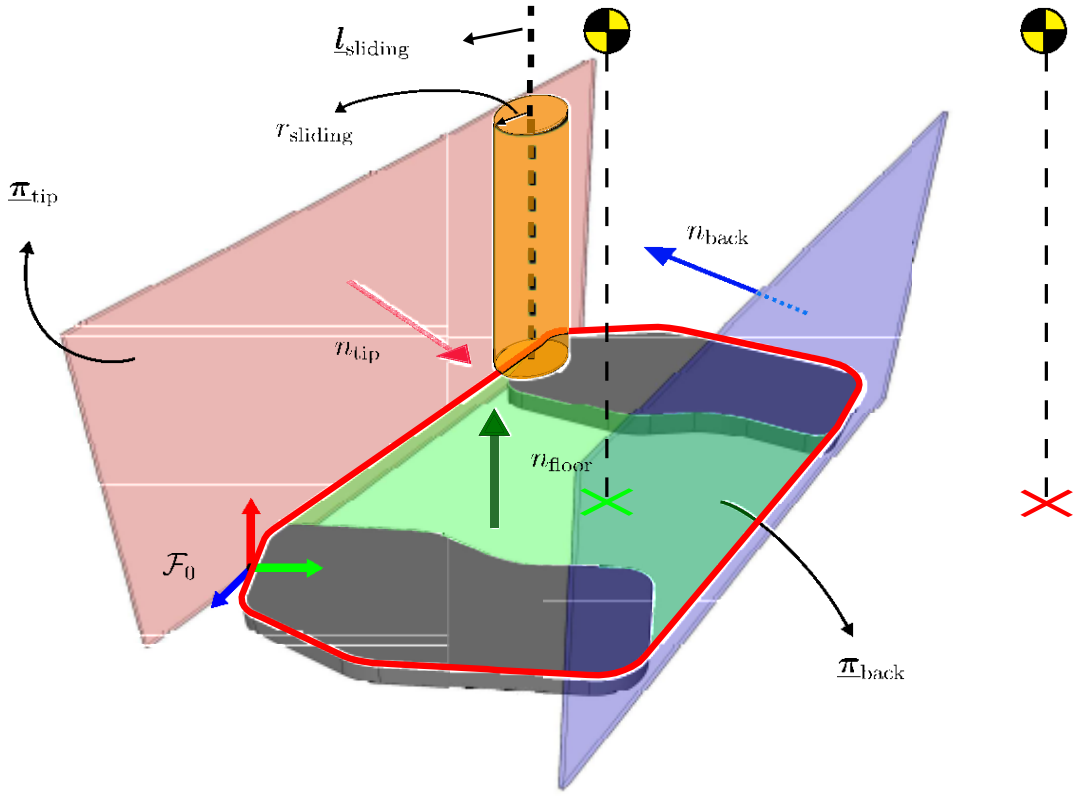

Figure 4.4: The DSP original SP is composed of feet area in *gray* and the area between feet in *light green*. The convex hull area is delimited by the *red* line, but we model the SP as two planes touching the tip ($\underline{\boldsymbol{\pi}}_{\text{tip}}$) in *pink* and the back ($\underline{\boldsymbol{\pi}}_{\text{back}}$) of feet in *blue*. The cylinder with radius r_{sliding}, constraining the sliding of the right foot, is on the tip of the right foot. When the CoM projection is inside the planes, shown by the green cross, the robot is statically stable; when outside, as shown by the red cross, the robot is not statically stable. The floor plane is represented by the *light green* plane and its normal is given by the *dark green* arrow.

4.6 Single Support Phase

The second phase in the walking cycle is the SSP. In the SSP, the robot foot swings from the back to the front to reach the desired location. The SP is composed of the sole of the support foot. We model the SP as the intersection of an infinite vertical cylinder with the ground plane, as shown in Figure 4.5. Although more conservative than the original SP, which is given by the support foot's convex hull, this new SP is fast to compute within the constrained control law presented in Chapter 5. An infinite cylinder is completely defined by the center line $\underline{\boldsymbol{l}}$ and the cylinder radius r_{CoM}, given a pure quaternion $\boldsymbol{l}$ that defines the line direction and an arbitrary point $\boldsymbol{p}$ on the line, $\underline{\boldsymbol{l}} \triangleq \boldsymbol{l} + \varepsilon\,(\boldsymbol{p} \times \boldsymbol{l})$ (Adorno, 2017). Therefore, the infinite cylinder is defined as the pair $(\underline{\boldsymbol{l}}_{\text{CoM}}, r_{\text{CoM}})$. The support phases alternates during the cicle and the cicle repeats until the robot reaches the final position.

Besides the support phase constraints showed in this section and in Section 4.5, we define in Section 4.7 additional constraints on the foot related to the contact to the floor and pelvis height.

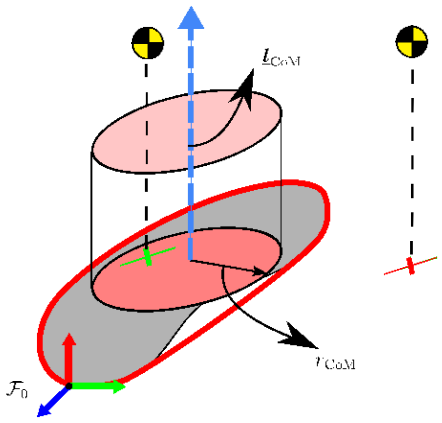

Figure 4.5: The SSP convex hull is the area delimited by the *red* line, but the SP is simplified to the *pink* area determined by the intersection between the infinite cylinder $(\underline{\boldsymbol{l}}_{\text{CoM}}, r_{\text{CoM}})$ and the ground plane. When the CoM is inside the SP, shown by the *green* cross, the robot is statically stable; when outside, as shown by the *red* cross, the robot is not statically stable.

4.7 Additional constraints

In addition to the aforementioned constraints, which are enforced to maintain a stable gait, other constraints also play an important role to enhance the overall behavior. For instance, Figure 4.4 shows the circular region formed by the intersection between a vertical cylinder and the ground plane $\underline{\boldsymbol{\pi}}_{\text{ground}}$. During the DSP, when the base frame $(\mathcal{F}_0)$ is on the left foot, the right foot tip is allowed to slide inside that circular region, giving more freedom to the robot gait. Conversely, when the base frame is on the right foot, a similar region is defined for the left foot. Also, we enforce the feet to stay on the ground plane at all times

during the DSP. These constraints are necessary because we control only the CoM, which means the end foot can rise above the floor and move around when controlling the CoM. Although the foot could be constrained to a point, constraining it into the circular region provides a much less conservative solution.

Moreover, a horizontal plane (see Figure 4.6) is also used to keep the pelvis above a minimum height, d_{pelvis}, during the whole walking cycle, hence preventing the robot from squatting.

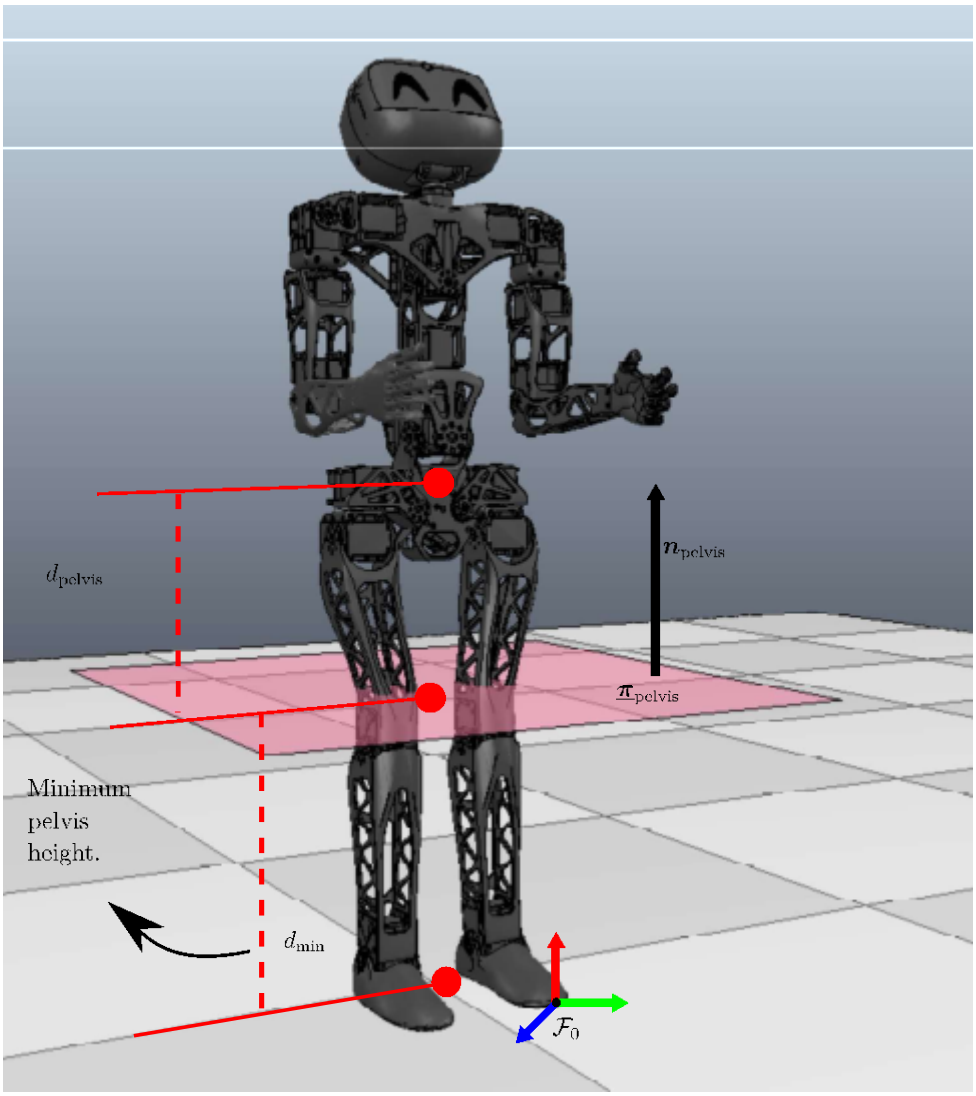

Figure 4.6: Pelvis plane $\underline{\boldsymbol{\pi}}_{\text{pelvis}}$ with normal $\boldsymbol{n}_{\text{pelvis}}$ and distance d_{pelvis} from the reference frame.

Last, the angles of the robot joints are constrained during the complete walking cycle to respect their mechanical limits, such that the minimum and maximum values for the joints are $\boldsymbol{q}_{\text{min}}, \boldsymbol{q}_{\text{max}} \in \mathbb{R}^n$.

4.8 Bipedal Model

Addicionally to the support phases and the constraints aforementioned, in order to perform a quasi-static gait in which the projection of the CoM onto the ground must always be kept inside the SP, only the kinematic model is necessary. To that aim, we consider the mechanism composed of the two legs. First, we define the support foot as the first link in the kinematic chain, and then attach the first link of the swing leg to the last link of the support leg in a process called *serialization* (Adorno, 2011), as shown on the *left* of Figure 4.7. For instance, let the left leg be the support leg and its forward kinematics with respect to $\mathcal{F}_0$ be given by $\underline{\boldsymbol{x}}_{\text{left}} \triangleq \underline{\boldsymbol{x}}_{\text{left}}(\boldsymbol{q}_{\text{left}})$, as shown in Figure 4.7, where $\boldsymbol{q}_{\text{left}} \in \mathbb{R}^n$ is the configuration vector of the left leg. Analogously, the forward kinematics of the right leg with respect $\mathcal{F}_6$ is given by $\underline{\boldsymbol{x}}_{\text{right}} \triangleq \underline{\boldsymbol{x}}_{\text{right}}\left(\boldsymbol{q}_{\text{right}}\right)$. The pose of the swing foot with respect to the support foot is given by $\underline{\boldsymbol{x}}_{\text{swing},r} = \underline{\boldsymbol{x}}^*_{\text{left}}\underline{\boldsymbol{x}}^5_6\underline{\boldsymbol{x}}_{\text{right}}$, where $\underline{\boldsymbol{x}}^5_6$ is transformation from frame $\mathcal{F}_5$ to frame $\mathcal{F}_6$ and the corresponding differential forward kinematics of the whole chain is given by $\text{vec}_8\, \dot{\underline{\boldsymbol{x}}}_{\text{swing},r} = \boldsymbol{J}_{\text{swing},r}\dot{\boldsymbol{q}}_r$, where $\boldsymbol{q}_r = \begin{bmatrix}\boldsymbol{q}^T_{\text{left}} & \boldsymbol{q}^T_{\text{right}}\end{bmatrix}^T \in \mathbb{R}^{2n}$ (Adorno, 2011) and thus $\boldsymbol{J}_{\text{swing},r} \in \mathbb{R}^{8\times 2n}$. Analogously, when the right and left feet are the support and swing feet, respectively, we obtain $\underline{\boldsymbol{x}}_{\text{swing},l} = \underline{\boldsymbol{x}}^*_{\text{right}}\underline{\boldsymbol{x}}^6_5\underline{\boldsymbol{x}}_{\text{left}}$, with $\text{vec}_8\, \dot{\underline{\boldsymbol{x}}}_{\text{swing},l} = \boldsymbol{J}_{\text{swing},l}\dot{\boldsymbol{q}}_l$, where $\boldsymbol{q}_l = \begin{bmatrix}\boldsymbol{q}^T_{\text{right}} & \boldsymbol{q}^T_{\text{left}}\end{bmatrix}^T$. With the bipedal model we can derive the CoM model shown in Section 4.9.

4.9 CoM Position and CoM Jacobian

To calculate the CoM, we analyze the relationship between a link CoM and the joint that moves it, which involves two relevant transformations, as shown in Figure 4.7. The first is the transformation $\underline{\boldsymbol{x}}^0_i(\boldsymbol{q})$ from the reference frame $\mathcal{F}_0$ to frame $\mathcal{F}_i$ at the end of the ith link. The second is the constant transformation $\underline{\boldsymbol{x}}^i_{c_i}$ from frame $\mathcal{F}_i$ to the frame $\mathcal{F}_{c_i}$ at the CoM of the ith link. Therefore, the transformation between frames $\mathcal{F}_i$ and $\mathcal{F}_{c_i}$ is given by

$$\underline{\boldsymbol{x}}^0_{c_i} = \underline{\boldsymbol{x}}^0_i\underline{\boldsymbol{x}}^i_{c_i}. \tag{4.3}$$

The CoM Jacobian is obtained from the time derivative of (4.3) as

$$\begin{aligned}\text{vec}_8\, \dot{\underline{\boldsymbol{x}}}^0_{c_i} &= \bar{\boldsymbol{H}}_8\left(\underline{\boldsymbol{x}}^i_{c_i}\right)\text{vec}_8\, \dot{\underline{\boldsymbol{x}}}^0_i = \bar{\boldsymbol{H}}_8\left(\underline{\boldsymbol{x}}^i_{c_i}\right)\boldsymbol{J}_i\dot{\boldsymbol{q}}_i \\ &= \bar{\boldsymbol{J}}_{c_i}\dot{\boldsymbol{q}}_i = \underbrace{\begin{bmatrix}\bar{\boldsymbol{J}}_{c_i} & \boldsymbol{0}^{8\times n-i}\end{bmatrix}}_{\boldsymbol{J}_{c_i}}\dot{\boldsymbol{q}},\end{aligned} \tag{4.4}$$

where we used the fact that $\dot{\underline{\boldsymbol{x}}}^i_{c_i} = 0$, $\boldsymbol{J}_i \in \mathbb{R}^{8\times i}$ and $\boldsymbol{q}_i \in \mathbb{R}^i$ are the Jacobian and the joint velocities vector up to joint i, and $\bar{\boldsymbol{H}}_8 : \mathcal{H} \to \mathbb{R}^{8\times 8}$ is an operator that satisfies $\text{vec}_8\left(\underline{\boldsymbol{h}}_1\underline{\boldsymbol{h}}_2\right) = \bar{\boldsymbol{H}}_8\left(\underline{\boldsymbol{h}}_2\right)\text{vec}_8\,\underline{\boldsymbol{h}}_1$ (Adorno, 2017). Moreover, the CoM position of the chain

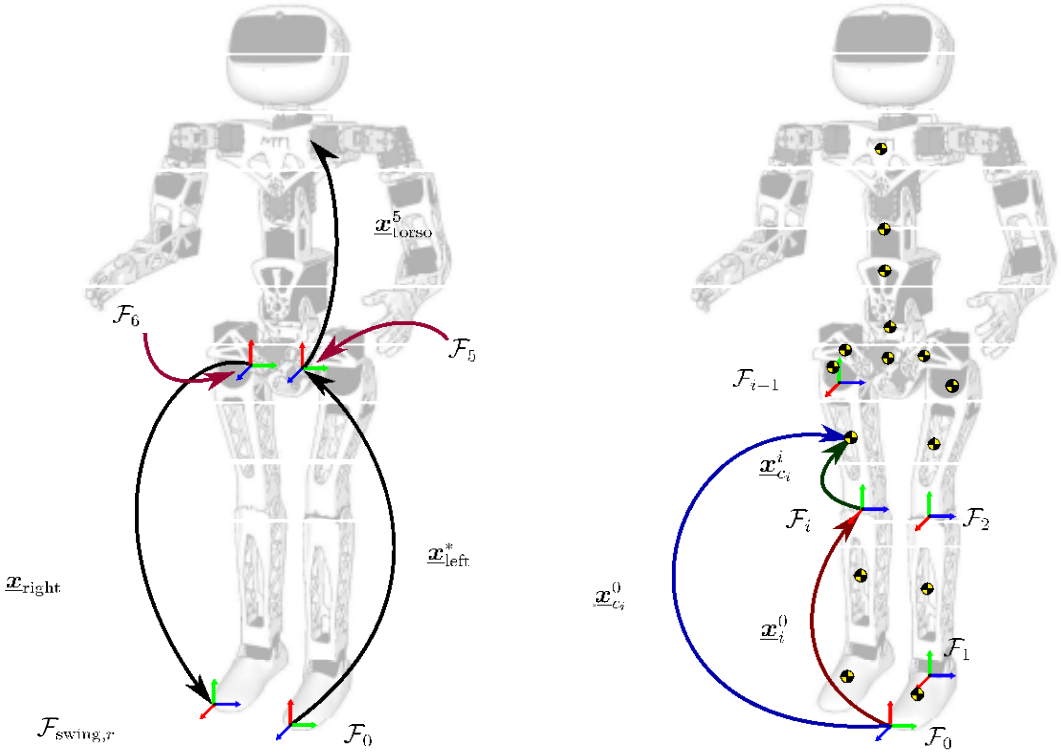

Figure 4.7: Biped robot: on the *left* the robot serialization, in which the first chain is the reversed left leg chain ($\underline{\boldsymbol{x}}^*_{\text{left}}$), followed by the transformation ($\underline{\boldsymbol{x}}^5_6$) from frame $\mathcal{F}_5$ to frame $\mathcal{F}_6$—attached to the bases of the left and right legs, respectively—, followed by the right leg chain ($\underline{\boldsymbol{x}}_{\text{right}}$); on the *right*, the CoM position of all links that are used to calculate the CoM of the whole kinematic chain composed of the two legs.

composed of the two legs and the pelvis, which has N degrees of freedom, is given by the weighted sum (Oliveira & Adorno, 2015)

$$\operatorname{vec}_3 \boldsymbol{p}_{\text{CoM}} = \frac{1}{M} \sum_{i-0}^{N} m_i \operatorname{vec}_3 \boldsymbol{p}_{c_i}, \tag{4.5}$$

where m_i is the mass of the ith link, $\boldsymbol{p}_{c_i}$ is the translational part of $\underline{\boldsymbol{x}}^0_{c_i}$, and M is the total mass of the mechanism. The CoM of the support foot, $\boldsymbol{p}_{c_0}$, is also taken into account because it contributes to the total mass of the mechanism. Finally, obtaining the translational component $\boldsymbol{J}_{p_{ci}}$ of $\boldsymbol{J}_{c_i}$ that satisfies $\operatorname{vec}_3 \dot{\boldsymbol{p}}_{c_i} = \boldsymbol{J}_{p_{c_i}} \dot{\boldsymbol{q}}$, as described in Section 3.2, we obtain

$$\operatorname{vec}_3 \dot{\boldsymbol{p}}_{\text{CoM}} = \frac{1}{M} \sum_{i-0}^{N} m_i \operatorname{vec}_3 \dot{\boldsymbol{p}}_{c_i} = \underbrace{\left(\frac{1}{M} \sum_{i-0}^{N} m_i \boldsymbol{J}_{p_{c_i}} \right)}_{\boldsymbol{J}_{\text{CoM}}} \dot{\boldsymbol{q}}, \tag{4.6}$$

where $\boldsymbol{J}_{\text{CoM}} \in \mathbb{R}^{3 \times n}$ is the CoM Jacobian of the complete chain.

4.10 Chapter Summary

In this chapter, we recalled the concept of ZMP and related it with the CoP and the CoM. We also presented the support phases and the corresponding constraints, and the additional constraints related to the swinging foot, the pelvis and the joints limits. We finally derived the bipedal model and the robot CoM position and Jacobian.

Now that we have the models and the constraints defined, we will derive the controllers for the walking task in Chapter 5.

5 Constrained Controller

In this chapter, we use the bipedal model, the gait model, the phases' additional constraints, the CoM position, and Jacobian from Chapter 4 to derive the two controllers we use during the complete cycle.

5.1 Constrained Controller Framework

To control the gait while respecting all the constraints, we use a constrained kinematic controller based on quadratic programming, where all the nonlinear geometric constraints are enforced as linear differential inequalities on the control inputs, the so-called vector field inequalities (Marinho et al., 2019).

The control input $\boldsymbol{u}$ is given by

$$\begin{aligned} \boldsymbol{u} \in \underset{\dot{\boldsymbol{q}}}{\operatorname{argmin}} \quad & \left\| \boldsymbol{J}_{\text{task}}(\boldsymbol{q})\dot{\boldsymbol{q}} + \eta\tilde{\boldsymbol{x}}_{\text{task}} \right\|_2^2 + \lambda^2 \left\| \dot{\boldsymbol{q}} \right\|_2^2 \\ \text{subject to} \quad & \boldsymbol{W}\dot{\boldsymbol{q}} \leq \boldsymbol{w} \\ & \boldsymbol{W}_{\text{eq}}\dot{\boldsymbol{q}} = \boldsymbol{w}_{\text{eq}}, \end{aligned} \tag{5.1}$$

where $\tilde{\boldsymbol{x}}_{\text{task}}$ is the task-space error vector, $\boldsymbol{J}_{\text{task}}(\boldsymbol{q})$ is the task Jacobian matrix, $\boldsymbol{q} \in \mathbb{R}^n$ is the joint vector, $\eta \in (0, \infty)$ is the controller gain, and $\lambda \in (0, \infty)$ is a damping factor to ensure that the joints velocities are minimized. Furthermore, the matrix $\boldsymbol{W} \in \mathbb{R}^{m \times n}$ and the vector $\boldsymbol{w} \in \mathbb{R}^m$ define the inequality constraints, whereas $\boldsymbol{W}_{\text{eq}} \in \mathbb{R}^{l \times n}$ and $\boldsymbol{w}_{\text{eq}} \in \mathbb{R}^l$ define the equality constraints.

The main idea of the vector field inequalities, which are used in the inequality constraints, is to define a differentiable function $d : \mathbb{R}^n \to \mathbb{R}$ that provides the (signed) distance between two geometric primitives as a function of the robot joints. Therefore, given a constant reference distance d_{ref} and $\tilde{d}(\boldsymbol{q}) \triangleq d(\boldsymbol{q}) - d_{\text{ref}}$, it is possible to show that the inequality $\dot{\tilde{d}}(\boldsymbol{q}) \geq -\eta_d \tilde{d}(\boldsymbol{q})$, where $\eta_d \in (0, \infty)$, ensures that, if $\tilde{d}(\boldsymbol{q}(0)) \geq 0$ then $\tilde{d}(\boldsymbol{q}(t)) \geq e^{-\eta_d t}\tilde{d}(\boldsymbol{q}(0)) \geq 0$ for all $t \geq 0$. Conversely, when the inequality is reversed, that is $\dot{\tilde{d}}(\boldsymbol{q}) \leq -\eta_d \tilde{d}(\boldsymbol{q})$, if $\tilde{d}(\boldsymbol{q}(0)) \leq 0$ then $\tilde{d}(\boldsymbol{q}(t)) \leq e^{-\eta_d t}\tilde{d}(\boldsymbol{q}(0)) \leq 0$ for all $t \geq 0$ (Marinho et al., 2019). Taking the time derivative from the distance function $\tilde{d}(\boldsymbol{q})$, we obtain $\dot{\tilde{d}}(\boldsymbol{q}) = \boldsymbol{J}_d \dot{\boldsymbol{q}}$, where $\boldsymbol{J}_d \triangleq \partial \tilde{d}(\boldsymbol{q})/\partial \boldsymbol{q}$ and can be used in (5.1).

What determines the type of differential inequality to be used—i.e., positive ($\geq$) or negative distances ($\leq$)—depends on the relationship between the geometric primitives. Given a point and a plane, a positive distance determines that the point is on the side of the plane to where its normal is pointing. For instance, in Figure 4.4, both normals $\boldsymbol{n}_{\text{tip}}$ and $\boldsymbol{n}_{\text{back}}$ points to the convex hull. Therefore, the distances between the green CoM projection and the planes are both positive. On the other hand, the distance of the red CoM projection to $\underline{\boldsymbol{\pi}}_{\text{tip}}$ is positive, but the distance to $\underline{\boldsymbol{\pi}}_{\text{back}}$ is negative. Analogously, the distance between a point inside a cylinder and the cylinder boundary is negative, whereas the distance between a point outside the cylinder and the cylinder boundary is positive.

On the other hand, an equality constraint such as $\dot{\tilde{d}} = -\eta \tilde{d}$ determines that the distance between the geometric primitives will converge exponentially to zero.

Therefore, the main challenge is to define suitable task variables $\boldsymbol{J}_{\text{task}}(\boldsymbol{q})$ and $\tilde{\boldsymbol{x}}_{\text{task}}$ and the corresponding constraint variables $\boldsymbol{W}, \boldsymbol{w}, \boldsymbol{W}_{\text{eq}}, \boldsymbol{w}_{\text{eq}}$ based on the geometrical primitives and control objectives described in Section 4. In Sections 5.2 and 5.3, we define the task variables for the DSP and the SSP, respectively.

5.2 DSP controller

From Section 4.5, during the DSP, the goal is to transfer the CoM projection from one foot to the other while it is between the planes $\underline{\boldsymbol{\pi}}_{\text{tip}}$ and $\underline{\boldsymbol{\pi}}_{\text{back}}$. In addition, both feet are on the ground plane $\underline{\boldsymbol{\pi}}_{\text{ground}}$, the tip of the end foot (i.e., the one to where the CoM projection is being moved) is confined to the cylinder $(\boldsymbol{l}_{\text{sliding}}, r_{\text{sliding}})$, the pelvis is above the plane $\underline{\boldsymbol{\pi}}_{\text{pelvis}}$, and the joint angles are limited by the joint range $[-\phi_{\text{safe},i}, \phi_{\text{safe},i}]$ for every ith joint. Using the signed distance functions and the corresponding Jacobians proposed by Marinho et al. (2019), namely the distance between points and cylinders and between points and planes, we define the following constraints to

- allow the swinging foot to sliding inside a cilynder:

$$\dot{\tilde{d}}_{\text{sliding}} = \boldsymbol{J}_{\text{sliding}} \dot{\boldsymbol{q}} \leq -\eta_{\text{sliding}} \tilde{d}_{\text{sliding}} = w_{\text{sliding}}, \tag{5.2}$$

where $\tilde{d}_{\text{sliding}}$ is the signed distance between the end-foot tip and the sliding cylinder $(\boldsymbol{l}_{\text{sliding}}, r_{\text{sliding}})$ such that a negative distance means that the point is inside the cylinder, the gain $\eta_{\text{sliding}} \in (0, \infty)$ determines how fast the cylinder boundary can be approached from the inside, and $\mathbb{R}^{1\times n} \ni \boldsymbol{J}_{\text{sliding}} = \partial\tilde{d}_{\text{sliding}}(\boldsymbol{q})/\partial\boldsymbol{q}$,where n is the robot's number of degree of freedom (DoF), in our case, n_{left} from the left leg and n_{right} from the right leg, a total of $n = n_{\text{left}} + n_{\text{right}}$;

- keep the foot on the floor:

$$\dot{\tilde{d}}_{\text{ground}} + \eta_{\text{ground}}\tilde{d}_{\text{ground}} = 0 \implies -\boldsymbol{J}_{\text{ground}}\dot{\boldsymbol{q}} = \eta_{\text{ground}}\tilde{d}_{\text{ground}} = w_{\text{ground}}, \tag{5.3}$$

where $\tilde{d}_{\text{ground}}$ is the signed distance between the end-foot tip and the ground plane $\underline{\boldsymbol{\pi}}_{\text{ground}}$, the gain $\eta_{\text{ground}} \in (0, \infty)$ determines how fast the foot should return to the ground in case it raises above the ground plane, and $\mathbb{R}^{1\times n} \ni \boldsymbol{J}_{\text{ground}} = \partial\tilde{d}_{\text{ground}}(\boldsymbol{q})/\partial\boldsymbol{q}$;

- keep the CoM from going beyond the feet's tip:

$$\dot{\tilde{d}}_{\text{tip}} \geq -\eta_{\text{tip}}\tilde{d}_{\text{tip}} \implies -\boldsymbol{J}_{\text{tip}}\dot{\boldsymbol{q}} \leq \eta_{\text{tip}}\tilde{d}_{\text{tip}} = w_{\text{tip}}, \tag{5.4}$$

where $\tilde{d}_{\text{tip}}$ is the signed distance between the CoM projection and the tip plane $\underline{\boldsymbol{\pi}}_{\text{tip}}$, the gain $\eta_{\text{tip}} \in \mathbb{R}$ determines how fast the CoM projection is allowed to approach the tip plane from its positive side (i.e., the side where the plane normal points at), and $\mathbb{R}^{1\times n} \ni \boldsymbol{J}_{\text{tip}} = \partial\tilde{d}_{\text{tip}}(\boldsymbol{q})/\partial\boldsymbol{q}$;

- keep the CoM from going beyond the feet's back:

$$\dot{\tilde{d}}_{\text{back}} \geq -\eta_{\text{back}}\tilde{d}_{\text{back}} \implies -\boldsymbol{J}_{\text{back}}\dot{\boldsymbol{q}} \leq \eta_{\text{back}}\tilde{d}_{\text{back}} = w_{\text{back}}, \tag{5.5}$$

where $\tilde{d}_{\text{back}}$ is the signed distance between the CoM projection and the back plane $\underline{\boldsymbol{\pi}}_{\text{back}}$, the gain $\eta_{\text{back}} \in \mathbb{R}$ determines how fast the CoM projection is allowed to approach the back plane from its positive side, and $\mathbb{R}^{1\times n} \ni \boldsymbol{J}_{\text{back}} = \partial\tilde{d}_{\text{back}}(\boldsymbol{q})/\partial\boldsymbol{q}$;

- keep the pelvis above the limit pelvis' height:

$$\dot{\tilde{d}}_{\text{pelvis}} \geq -\eta_{\text{pelvis}}\tilde{d}_{\text{pelvis}} \Longrightarrow -\boldsymbol{J}_{\text{pelvis}}\dot{\boldsymbol{q}} \leq \eta_{\text{pelvis}}\tilde{d}_{\text{pelvis}} = w_{\text{pelvis}}, \tag{5.6}$$

where $\tilde{d}_{\text{pelvis}}$ is the signed distance between the pelvis position and the pelvis plane $\underline{\boldsymbol{\pi}}_{\text{pelvis}}$, the $\eta_{\text{pelvis}} \in \mathbb{R}$ determines how fast the CoM is allowed to approach the pelvis plane from above, and $\mathbb{R}^{1\times n} \ni \boldsymbol{J}_{\text{tip}} = \partial\tilde{d}_{\text{tip}}(\boldsymbol{q})/\partial\boldsymbol{q}$; and, finally,

- keep the joints' angles inside the minimum and maximum limits:

$$\dot{\boldsymbol{q}} \leq -\eta_{\phi}(\boldsymbol{q} - \boldsymbol{q}_{\max}) = \boldsymbol{w}_{\phi_{\max}}, \tag{5.7}$$

$$-\dot{\boldsymbol{q}} \leq \eta_{\phi}(\boldsymbol{q} - \boldsymbol{q}_{\min}) = \boldsymbol{w}_{\phi_{\min}}, \tag{5.8}$$

where $\boldsymbol{q}_{\min}, \boldsymbol{q}_{\max} \in \mathbb{R}^n$ are the vectors of minimum and maximum values for the joints.

The goal during DSP is to transfer the CoM projection between the feet, which means to control only the x and y coordinates of the CoM. Therefore, in order to generate the control input (5.1), we define $\boldsymbol{J}_{\text{task}} \triangleq \boldsymbol{J}_{\text{CoM}_{(x,y)}}$, where $\boldsymbol{J}_{\text{CoM}_{(x,y)}}$ is given by the first and second rows of $\boldsymbol{J}_{\text{CoM}}$ in (4.6). In addition, $\tilde{\boldsymbol{x}}_{\text{task}} \triangleq I_{2\text{x}3}\,\text{vec}_3(\boldsymbol{p}_{\text{CoM}} - \boldsymbol{p}_{\text{CoM}d})$ with $\boldsymbol{p}_{\text{CoM}d}$ being the desired CoM position, $\boldsymbol{p}_{\text{CoM}}$ being its current value, and

$$I_{2\text{x}3} \triangleq \begin{bmatrix} 1 & 0 & 0 \\ 0 & 1 & 0 \end{bmatrix}.$$

Furthermore, the constraint variables are defined as

$$\begin{aligned} \boldsymbol{W} &= \begin{bmatrix} \boldsymbol{J}_{\text{sliding}}^T & -\boldsymbol{J}_{\text{tip}}^T & -\boldsymbol{J}_{\text{back}}^T & -\boldsymbol{J}_{\text{pelvis}}^T & \boldsymbol{I}_n & -\boldsymbol{I}_n \end{bmatrix}^T, \\ \boldsymbol{w} &= \begin{bmatrix} w_{\text{sliding}} & w_{\text{tip}} & w_{\text{back}} & w_{\text{pelvis}} & \boldsymbol{w}_{\phi_{\max}}^T & \boldsymbol{w}_{\phi_{\min}}^T \end{bmatrix}^T, \\ \boldsymbol{W}_{\text{eq}} &= -\boldsymbol{J}_{\text{ground}}, \\ \boldsymbol{w}_{\text{eq}} &= w_{\text{ground}}. \end{aligned}$$

To guarantee the next phase feasiblility, we finish the current phase with all the constrained entities inside the allowed region for the next phase. We selected, for instance, the desired CoM of the DSP inside the next SSP's support polygon. Fig. 5.1 shows a moment of the current DSP. The gray rectangles represents the feet's contact area to the floor, the dashed red line the current SP, the pink line the feet's tip plane projection to the floor, the blue line the feet's back plane projection to the floor, the black circle the interssection of the cylinfer border with the floor, and the black point represents the current CoM's projection, p_{CoM}. The objective in the current phase is to transfer the CoM to anywhere inside the circle. Therefore for the next SSP the CoM already starts inside the allowed region, the next SP.

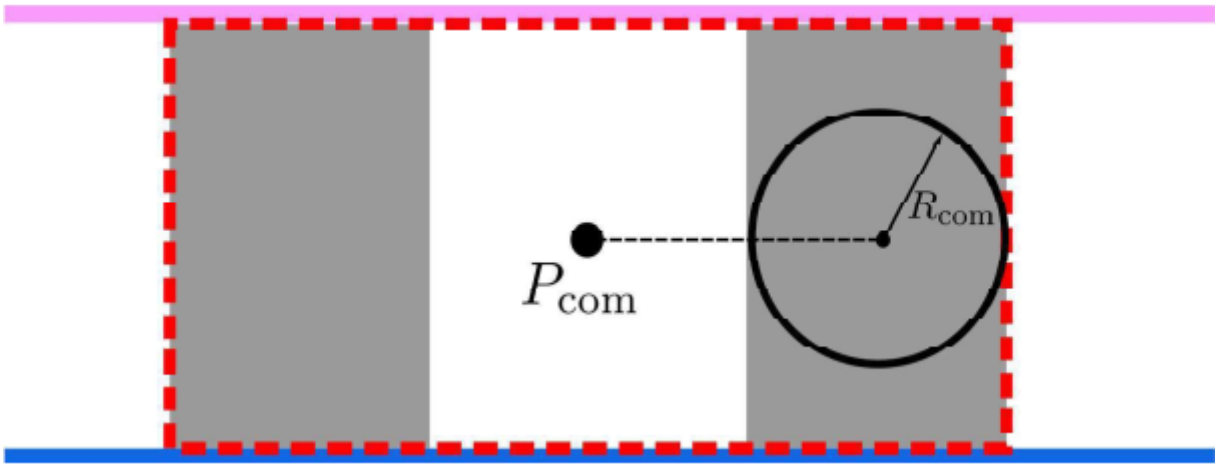

Figure 5.1: Current and next phase support polygon.

5.3 SSP controller

During the SSP, the goal is to place the end foot to the next location while the CoM projection is inside the cylinder $(\underline{\boldsymbol{l}}_{\text{CoM}}, r_{\text{CoM}})$. As in the DSP, in the SSP, the pelvis is above the plane $\underline{\boldsymbol{\pi}}_{\text{pelvis}}$, and the ith joint angle is inside the interval $[-\phi_{\text{safe},i}, \phi_{\text{safe},i}]$ for every joint. Also, we define the constraint

$$\dot{\tilde{d}}_{\text{CoM}} = \boldsymbol{J}_{\text{CoM}}\dot{\boldsymbol{q}} \leq -\eta_{\text{CoM}}\tilde{d}_{\text{CoM}} = w_{\text{CoM}}, \tag{5.9}$$

where $\tilde{d}_{\text{CoM}}$ is the signed distance between the CoM projection and the support polygon cylinder $(\underline{\boldsymbol{l}}_{\text{CoM}}, r_{\text{CoM}})$ such that a negative distance means that the CoM projection is inside the support polygon, the gain $\eta_{\text{CoM}} \in (0, \infty)$ determines how fast the CoM projection can approach the SP boundary, and $\mathbb{R}^{1\times n} \ni \boldsymbol{J}_{\text{CoM}} = \partial\tilde{d}_{\text{CoM}}(\boldsymbol{q})/\partial\boldsymbol{q}$. The additional constraints are given by (5.6) and (5.7), respectively. Therefore,

$$\boldsymbol{W} = \begin{bmatrix} \boldsymbol{J}_{\text{CoM}}^T & -\boldsymbol{J}_{\text{pelvis}}^T & \boldsymbol{I}_n & -\boldsymbol{I}_n \end{bmatrix}^T$$

and $\boldsymbol{w} = \begin{bmatrix} w_{\text{CoM}} & w_{\text{pelvis}} & \boldsymbol{w}_{\phi_{\max}}^T & \boldsymbol{w}_{\phi_{\min}}^T \end{bmatrix}^T$.

Since in the SSP the goal is to swing the end foot from the current position to a forward position, the control input is generated using (5.1), where $\boldsymbol{J}_{\text{task}} \triangleq \boldsymbol{J}_{\text{swing},r}$ is the Jacobian matrix of the coupled kinematic chain composed of the left leg followed by the right leg, when the base frame is on the left foot, and $\tilde{\boldsymbol{x}}_{\text{task}} \triangleq \text{vec}_8\left(\underline{\boldsymbol{x}}_{\text{swing},r} - \underline{\boldsymbol{x}}_{d,r}\right)$, where $\underline{\boldsymbol{x}}_{\text{swing},r}$ is the right-foot pose and $\underline{\boldsymbol{x}}_d$ is its desired value. Analogously, when the base frame is on the right foot, $\boldsymbol{J}_{\text{task}} \triangleq \boldsymbol{J}_{\text{swing,l}}$ and $\tilde{\boldsymbol{x}}_{\text{task}} \triangleq \text{vec}_8\left(\underline{\boldsymbol{x}}_{\text{swing},l} - \underline{\boldsymbol{x}}_{d,l}\right)$, where $\boldsymbol{J}_{\text{swing,l}}$ is the Jacobian of the coupled kinematic chain composed of the right leg followed by the left leg and $\underline{\boldsymbol{x}}_{\text{swing},l}$ is the left-foot pose.

5.4 Chapter Summary

In this chapter, we define the controllers for both phases. We derive for the DSP the controller of the CoM with the appropriate constraints where the main objective is to transfer the CoM from the old support polygon to the new one, while both feet are on the floor. We also derive for the SSP the controller of the robot swing leg with the appropriate constraints where the main objective is to swing one leg forward while the other foot remains touching the floor. The results of the complete cycle control are shown in Chapter 6.

6 Simulation and Results

This chapter presents the simulation settings and the results of the simulation using our approach.

6.1 Simulation settings

We evaluated, in simulation, the control strategy for the complete walking cycle on the Poppy[1] humanoid legs using MATLAB software, DQ Robotics library (Adorno & Marinho, 2021), and V-REP (Rohmer et al., 2013) for visualization. All robot joints positions are equal to zero in the beginning of the first walking cycle. The CoM, end foot, base foot, and pelvis start inside the allowable regions to ensure the feasibility of (5.1). Since the robot is small, with foot width and length equal to 7 cm and 9.34 cm, respectively, we defined a small step length during SSP. More specifically, each step has 5 cm on the horizontal saggital axis. The controler and constraints parameters were chosen by error and trial. The controller parameters in (5.1) are $\eta = 0.05$ and $\lambda = 0.1$. The constraints were defined as described in Sections 5.2 and 5.3, with $\eta_{\text{sliding}} = 5$, $\eta_{\text{ground}} = 5$, $\eta_{\text{pelvis}} = 500$, $\eta_{\text{tip}} = 10$, $\eta_{\text{back}} = 20$, $\eta_{\phi} = 10$, and $\eta_{\text{CoM}} = 5$.

During the DSP, the geometrical constraints were defined as $\underline{\boldsymbol{\pi}}_{\text{ground}} = \hat{k}$, $(\boldsymbol{l}_{\text{sliding}}, r_{\text{sliding}}) = (\hat{k} + \varepsilon(\boldsymbol{p}_{\text{endtip}} \times \hat{k}), 0.035)$, where $\boldsymbol{p}_{\text{endtip}}$ is the end-foot tip position and the 0.035 is the radio in meters, and $\underline{\boldsymbol{\pi}}_{\text{pelvis}} = \hat{k} + \varepsilon 0.2$,where 0,2 is the heigth in meters. The $\underline{\boldsymbol{\pi}}_{\text{tip}}$ and $\underline{\boldsymbol{\pi}}_{\text{back}}$ were defined such that they are orthogonal to the ground plane and pass through points

[1] https://www.poppy-project.org/en/robots/poppy-humanoid

at both the feet tips and backs, respectively. During the SSP, the geometrical constraint related to the SP was defined as $(\underline{\boldsymbol{l}}_{\mathrm{CoM}}, r_{\mathrm{CoM}}) = (\hat{k} + \varepsilon(\boldsymbol{p}_{\mathrm{basecom}} \times \hat{k}), 0.045)$, where $\boldsymbol{p}_{\mathrm{basecom}}$ is the base foot CoM and 0.045 is the cilynder radio in meters.

The control objective is switched from the DSP to the SSP when the error stops decreasing and the CoM projection is within the SSP cylinder $(\underline{\boldsymbol{l}}_{\mathrm{CoM}}, r_{\mathrm{CoM}})$ of the end foot. Conversely, the control objective is switched from the SSP to the DSP when the error is below a threshold of 0.001. Adittionaly, when we achieve this error threshold we garantee that the ZMP is always inside the next phase support polygon. The same happens to the pelvis, the joints limits and the sliding foot. Therefore the next phase controler is always factible since every entity we constraint is inside the next allowed region.

In order to update the joints, a first-order numerical integration (Euler's method) is performed using an integration step of 0.005 s.

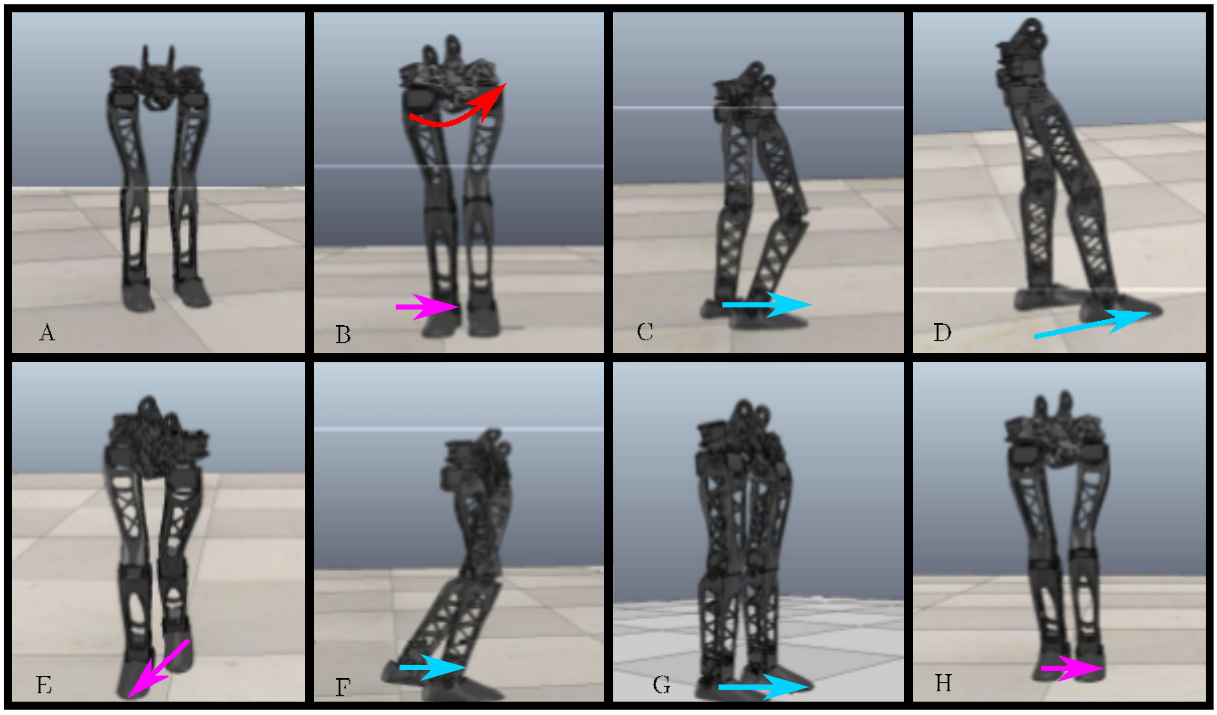

Figure 6.1: Complete cycle. A) Initial configuration (DSP); B) End of the DSP; C) the right foot swings towards the desired location, which is achieved in D; E) the CoM is transferred from the left SP to the right SP; F) the left foot swings toward the desired location, which is achieved in G; H), finally, the cycle starts again.

6.2 Closed-loop behavior of the complete walking cycle

Figure 6.1 shows the first complete walking cycle, in which the CoM projection was always confined to the SP, ensuring a stable gait. In the first DSP, the CoM projection started inside the SP, but outside both feet, and then it was transferred from the old to the new support foot. Figure 6.2A shows that this first part was completed with a

steady-state error as the CoM projection could not be driven to the desired value due to the constraints. Nonetheless, the CoM projection entered into the SP of the next SSP because the steady-state error was smaller than the threshold given by the *dashed-red* line, which represents the distance between the centerline and the boundary of the next SSP cylinder.

During the first DSP, the CoM projection was kept inside the SP, which is approximated by the region between the tip plane and back plane, as indicated by the positive distances to each plane, namely d_{tip} and d_{back} in Figs. 6.2D and E. The constraint on the end-foot tip was also obeyed, as the end-foot tip stayed inside the sliding cylinder, which is shown by the curve below the threshold in Figure 6.2B. The steady-state distance between the end-foot and the ground plane was approximately 0.01 mm due to discretization effects.

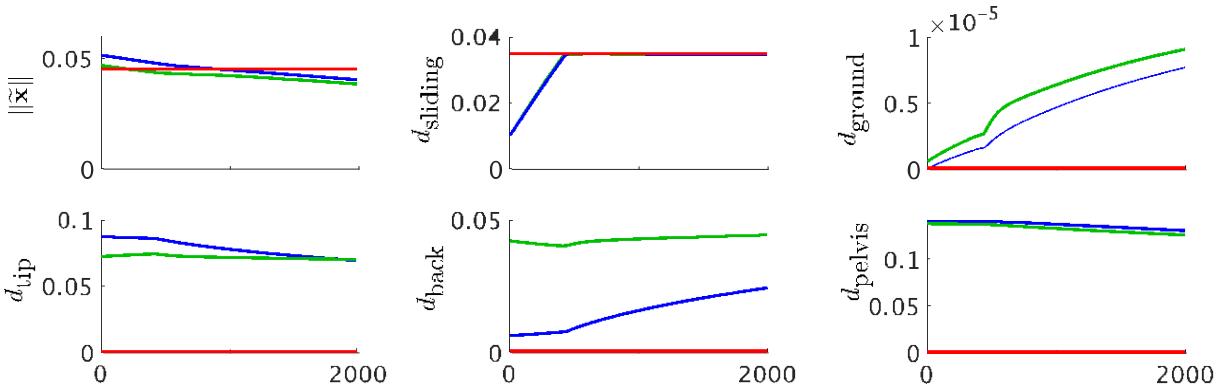

Figure 6.2: Time-response during the DSP for one complete cycle (first DSP in *blue* and second in *green*). A) the norm of the CoM projection error and the boundary of the next SSP in *dashed-red* line; B) end foot pose distance from sliding cylinder main axis with corresponding boundary in *dashed-red* line; *C*) foot pose distance from the floor plane; D) the distance of the CoM from the plane formed by feet tip; E) CoM distance from the plane formed by back tip; F) and distance of the pelvis to the plane.

Following the first DSP, the first SSP starts after the error in the DSP stops decreasing. Figure 6.3A shows that the swing foot (i.e. the right one) is placed at the desired location as the pose error norm decreases exponentially to zero. Moreover, the CoM was kept inside the SP during the entire SSP (Figure6.3B), as well as the pelvis was above the minimum height (Figure6.3C).

For the next DSP, the projection of the CoM was transferred from the left foot to the right foot and the behavior was analogous to the first behavior, as shown by the green curves in Figure 6.2. The second DSP is followed by the second SSP, in which the behavior was also analogous to the first SSP, as shown by the green curves in Figure 6.3.

Finally, Figure 6.4 shows that the joints limits were respected during the complete walking cycle.

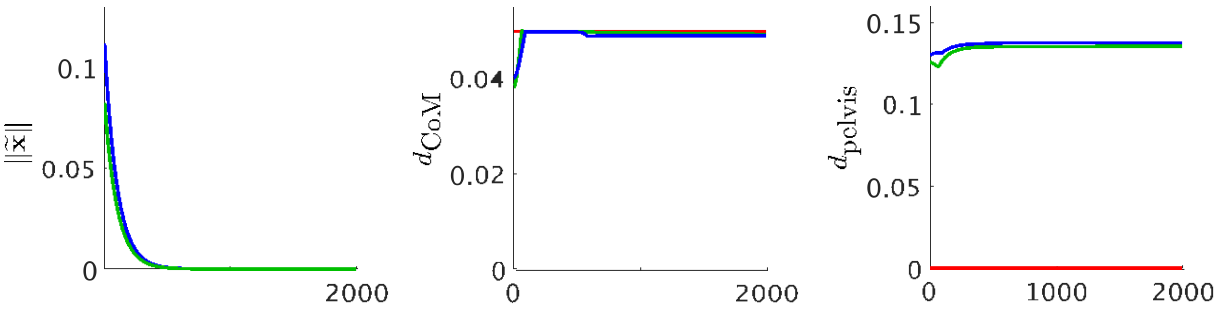

Figure 6.3: Time response during the first SSP (right leg, *blue curve*) and during the second SSP (the left leg, *green curve*). On the *left*, the foot pose error norm. In the *middle*, the distance of the CoM projection to the boundary of the SP, which is represented by the *dashed-red line* ($d_{\mathrm{CoM}} = 0$ means that the CoM is on the center of the SP). On the *right*, the distance of the pelvis to the minimum height allowed.

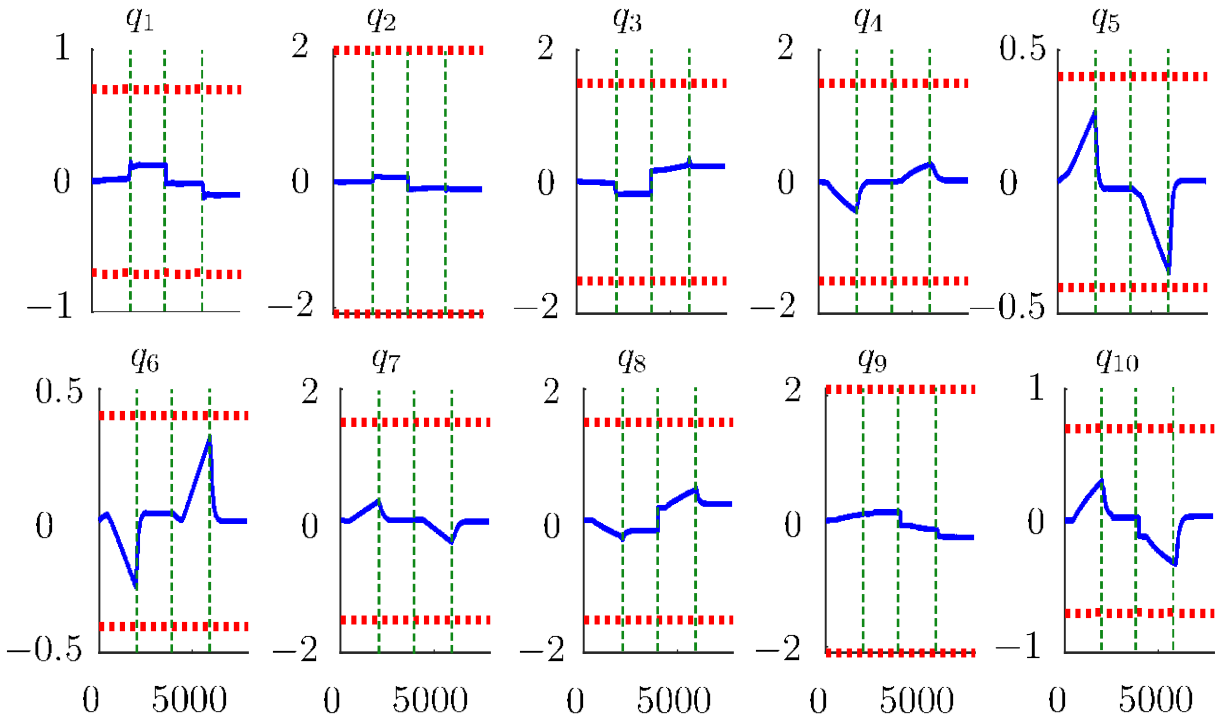

Figure 6.4: Joint angles during the complete gait cycle. The *vertical dashed lines* indicate the transition from DSP to SSP and from SSP to DSP. The *horizontal dashed lines* indicate the joint limits.

6.3 Chapter Summary

In this chapter, we showed a complete walking cicle: two DSPs and two SSPs. We showed that during the DSPs, the robot CoM was transfered to the next SP by entering the next phase SP, the CoM was kept inside the two planes constraining the SP, the swinging feet was inside the slidding cilynder and was not in contact with the floor plane due to discretization effects, and the pelvis was above the pelvis' plane. During the SSPs, the robot swinging foot achieved the desired position while the CoM was inside the SP cylinder and the pelvis was above the pelvis' plane. During the complete cycle the joints was inside the maximum and minimun limits. In Chapter 7, we will present our conslusions and detailed the next steps for a future work.

7 Conclusion and Future Works

7.1 Conclusions

This thesis has proposed a closed-loop constrained controller for the quasi-static bipedal walking based on quadratic programming and differential inequalities. The controller takes into account constraints on the joints, CoM, swing foot, and pelvis. The SP is modeled by using geometric primitives and the constraints are defined by using the differential inequalities associated to those primitives. This enables the control of the CoM, during the DSP, and the swing foot, during the SSP, without explicitly specifying the trajectory for the CoM. In addition, differently from classic approaches in which the CoM must follow a trajectory, our technique is less conservative as the CoM is bounded by the SP, but it does not follow any predefined trajectory. As a result, we do not need to calculate a CoM trajectory and the implementation is much simpler than the one proposed by Kajita et al. (2003).

All constraints were respected during the entire walking cycle, although the discretization played a relatively negligible role in the floor plane constraint. More specifically, during the DSP, both feet were supposed to stay flat on the ground, but disturbances from the discretization of the control signal would make the base foot raise up to 0.1 mm.

One disadvantage of our method is that closed-loop asymptotic stability is not guaranteed due to the constraints. Therefore, if the steps are too large, it may be the case that the closed-loop system reaches a local minimum and the step is not concluded. Nonetheless, the robot would not fall in those cases because the constraints ensure that the CoM

projection is always inside the SP, thus enforcing static balance. The quasi-static walking is also a disadvantage of our approach since it is slower than the other state-of-the-art works, which are based on dynamic walking. Besides, we did not study the system behavior in the presence of disturbances, as done in the work of Maximo et al. (2016). Therefore, we do not guarantee the robot balance under such circumstances.

7.2 Future works

Further works will focus on implementing the controller on the Poppy humanoid robot available at the Mechatronics, Control, and Robotics group at UFMG and the extension of our technique to dynamic gait.

Bibliography

Adhami, L. & Coste-Manirei, E. (2003). Optimal planning for minimally invasive surgical robots. *IEEE Trans. Robot. Autom.*, 19(5), 854–863.

Adolph, K. E. & Robinson, S. R. (2013). The Road to Walking. In P. D. Zelazo (Ed.), *Oxford Handb. Dev. Psychol. Vol. 1*, number April 2018 (pp. 402–444). Oxford University Press.

Adorno, B. (2017). Robot Kinematic Modeling and Control Based on Dual Quaternion Algebra – Part I: Fundamentals.

Adorno, B. V. (2011). *Two-arm Manipulation: From Manipulators to Enhanced Human-Robot Collaboration [Contribution à la manipulation à deux bras : des manipulateurs à la collaboration homme-robot]*. Ph.d. dissertation, Université Montpellier 2, Montpellier, France,.

Adorno, B. V., Fraisse, P., & Druon, S. (2010). Dual position control strategies using the cooperative dual task-space framework. In *2010 IEEE/RSJ Int. Conf. Intell. Robot. Syst.* (pp. 3955–3960).: IEEE.

Adorno, B. V. & Marinho, M. M. (2021). Dq robotics: A library for robot modeling and control. *IEEE Robotics & Automation Magazine*, 28, 102–116.

Akachi, K., Kaneko, K., Kanehira, N., Ota, S., Miyamori, G., Hirata, M., Kajita, S., & Kanehiro, F. (2005). Development of humanoid robot HRP-3P. In *5th IEEE-RAS International Conference on Humanoid Robots, 2005.*, volume 2005 (pp. 50–55).: IEEE.

Ambrose, R., Aldridge, H., Askew, R., Burridge, R., Bluethmann, W., Diftler, M., Lovchik, C., Magruder, D., & Rehnmark, F. (2000). Robonaut: NASA's space humanoid. *IEEE Intelligent Systems*, 15(4), 57–63.

Anderson, S., Wisse, M., Atkeson, C., Hodgins, J., Zeglin, G., & Moyer, B. (2005). Powered bipeds based on passive dynamic principles. In *5th IEEE-RAS International Conference on Humanoid Robots, 2005.* (pp. 110–116).

Barr, A. E., Safadi, F. F., Gorzelany, I., Amin, M., Popoff, S. N., & Barbe, M. F. (2003). Repetitive, Negligible Force Reaching in Rats Induces Pathological Overloading of Upper Extremity Bones. *J. Bone Miner. Res.*, 18(11), 2023–2032.

Bergeles, C. & Guang-Zhong Yang (2014). From Passive Tool Holders to Microsurgeons: Safer, Smaller, Smarter Surgical Robots. *IEEE Trans. Biomed. Eng.*, 61(5), 1565–1576.

Bertelsen, A., Melo, J., Sánchez, E., & Borro, D. (2013). A review of surgical robots for spinal interventions. *Int. J. Med. Robot. Comput. Assist. Surg.*, 9(4), 407–422.

Blickhan, R. (1989). The spring-mass model for running and hopping. *Journal of Biomechanics*, 22, 1217–1227.

Bluethmann, W., Ambrose, R., Diftler, M., Askew, S., Huber, E., Goza, M., Rehnmark, F., Lovchik, C., & Magruder, D. (2003). Robonaut: A robot designed to work with humans in space. *Autonomous Robots*, 14(2-3), 179–197.

Bohorquez, N. & Wieber, P.-B. (2018). Adaptive step rotation in biped walking. In *2018 IEEE/RSJ Int. Conf. Intell. Robot. Syst.* (pp. 720–725).: IEEE.

Chevallereau, C., Bessonnet, G., Abba, G., & Aoustin, Y. (2009). *Bipedal Robots: Modeling, Design and Walking Synthesis*. London, UK: ISTE.

Christensen, H. I. (2003). Intelligent Home Appliances. In *Robotics Research*, number 6 (pp. 319–327). Berlin, Heidelberg: Springer Berlin Heidelberg.

Davids, A. (2002). Urban search and rescue robots: from tragedy to technology. *IEEE Intell. Syst.*, 17(2), 81–83.

Diftler, M., Permenter, F., Hargrave, B., Platt, R., Savely, R., Ambrose, R., Mehling, J., Abdallah, M., Radford, N., Bridgwater, L., Sanders, A., Askew, R., Linn, D., & Yamokoski, J. (2011). Robonaut 2 - The first humanoid robot in space. In *2011 IEEE International Conference on Robotics and Automation*, volume 1 (pp. 2178–2183).: IEEE.

Englsberger, J., Werner, A., Ott, C., Henze, B., Roa, M. A., Garofalo, G., Burger, R., Beyer, A., Eiberger, O., Schmid, K., & Albu-Schaffer, A. (2014). Overview of the torque-controlled humanoid robot TORO. In *2014 IEEE-RAS International Conference on Humanoid Robots*, volume 2015-Febru (pp. 916–923).: IEEE.

Feng, S., Whitman, E., Xinjilefu, X., & Atkeson, C. G. (2015). Optimization-based Full Body Control for the DARPA Robotics Challenge. *J. F. Robot.*, 32(2), 293–312.

Fujita, M., Kuroki, Y., Ishida, T., & Doi, T. (2003). A small humanoid robot SDR-4X for entertainment applications. In *Proceedings 2003 IEEE/ASME International Conference on Advanced Intelligent Mechatronics (AIM 2003)*, volume 2 (pp. 938–943).: IEEE.

Fukuda, T., Dario, P., & Yang, G.-Z. (2017). Humanoid robotics-History, current state of the art, and challenges. *Science Robotics*, 2(13), 1–3.

Geyer, H., Seyfarth, A., & Blickhan, R. (2006). Compliant leg behaviour explains basic dynamics of walking and running. *Proceedings of the Royal Society B: Biological Sciences*, 273, 2861–2867.

Gouaillier, D., Hugel, V., Blazevic, P., Kilner, C., Monceaux, J., Lafourcade, P., Marnier, B., Serre, J., & Maisonnier, B. (2009). Mechatronic design of NAO humanoid. In *2009 IEEE International Conference on Robotics and Automation* (pp. 769–774).: IEEE.

Grizzle, J., Abba, G., & Plestan, F. (2001). Asymptotically stable walking for biped robots: analysis via systems with impulse effects. *IEEE Transactions on Automatic Control*, 46, 51–64.

Guarnieri, M. (2010). The Roots of Automation Before Mechatronics [Historical. *IEEE Ind. Electron. Mag.*, 4(2), 42–43.

Harari, Y. N. (2018). *Sapiens: Uma Breve História da Humanidade*. Porto Alegre: L&PM, 32 edition.

Hashimoto, S., Narita, S., Kasahara, H., Shirai, K., Kobayashi, T., Takanishi, A., Sugano, S., Yamaguchi, J., Sawada, H., Takanobu, H., Shibuya, K., Morita, T., Kurata, T., Onoe, N., Ouchi, K., Noguchi, T., Niwa, Y., Nagayama, S., Tabayashi, H., Matsui, I., Obata, M., Matsuzaki, H., Murasugi, A., Kobaysashi, H., Haruyama, S., Okada, T., Hidaki, Y., Taguchi, Y., Hoashi, K., Morikawa, E., Iwano, Y., Araki, D., Suzuki, J., Yokoyama, M., Dawa, I., Nishino, D., Inoue, S., Hirano, T., Soga, E., Gen, S., Yanada, T., Kato, K., Sakamoto, S., Ishii, Y., Matsuo, S., Yamamoto, Y., Sato, K., Hagiwara, T., Ueda, T., Honda, N., Hashimotoo, D., Hananmoto, T., Kayaba, S., Kojima, T., Iwata, H., Kubodera, H., Matsuki, R., Nakajima, T., Nitto, K., Yamammoto, D., Kamizaki, Y., Nagaike, S., & Kunitake, Y. (2002). Humanoid robots in Waseda University - Hadaly-2 and WABIAN. *Autonomous Robots*, 12(1), 25–38.

Herdt, A., Diedam, H., Wieber, P.-B., Dimitrov, D., Mombaur, K., & Diehl, M. (2010). Online Walking Motion Generation with Automatic Footstep Placement. *Adv. Robot.*, 24(5-6), 719–737.

Hirai, K., Hirose, M., Haikawa, Y., & Takenaka, T. (2007). The development of Honda humanoid robot. In *Proceedings. 1998 IEEE Int. Conf. Robot. Autom. (Cat. No.98CH36146)*, volume 2 (pp. 1321–1326).: IEEE.

Hirose, M. & Ogawa, K. (2007). Honda humanoid robots development. *Philosophical Transactions of the Royal Society A: Mathematical, Physical and Engineering Sciences*, 365(1850), 11–19.

Hirukawa, H., Kanehiro, F., Kaneko, K., Kajita, S., Fujiwara, K., Kawai, Y., Tomita, F., Hirai, S., Tanie, K., Isozumi, T., Akachi, K., Kawasaki, T., Ota, S., Yokoyama, K., Handa, H., Fukase, Y., ichiro Maeda, J., Nakamura, Y., Tachi, S., & Inoue, H. (2004). Humanoid robotics platforms developed in HRP. *Robotics and Autonomous Systems*, 48, 165–175.

Hunter, I. W., Hollerbach, J. M., & Ballantyne, J. (1991). A comparative analysis of actuator technologies for robotics. *Robotics Review*, 2, 299–342.

Ill-Woo Park, Jung-Yup Kim, Jungho Lee, & Jun-Ho Oh (2005). Mechanical design of humanoid robot platform KHR-3 (KAIST humanoid robot - 3: HUBO). In *5th IEEE-RAS International Conference on Humanoid Robots, 2005.*, volume 2005 (pp. 321–326).: IEEE.

Ishii, S., Tanaka, S., & Hiramatsu, F. (1995). Meal assistance robot for severely handicapped people. In *Proc. 1995 IEEE Int. Conf. Robot. Autom.*, volume 2 (pp. 1308–1313).: IEEE.

Kajita, S., Kanehiro, F., Kaneko, K., Fujiwara, K., Harada, K., Yokoi, K., & Hirukawa, H. (2003). Biped walking pattern generation by using preview control of zero-moment point. In *2003 IEEE Int. Conf. Robot. Autom. (Cat. No.03CH37422)*, volume 2 (pp. 1620–1626).: IEEE.

Kajita, S., Morisawa, M., Harada, K., Kaneko, K., Kanehiro, F., Fujiwara, K., & Hirukawa, H. (2006). Biped walking pattern generator allowing auxiliary ZMP control. In *2006 IEEE/RSJ International Conference on Intelligent Robots and Systems* (pp. 2993–2999).

Kajita, S., Nagasaki, T., Kaneko, K., Yokoi, K., & Tanie, K. (2004). A hop towards running humanoid biped. In *IEEE International Conference on Robotics and Automation, 2004. Proceedings. ICRA '04. 2004.*, volume 1 (pp. 629–635 Vol.1).

Kajita, S. & Tani, K. (1991). Study of dynamic biped locomotion on rugged terrain-derivation and application of the linear inverted pendulum mode. In *Proceedings. 1991 IEEE Int. Conf. Robot. Autom.*, volume 2 (pp. 1405–1411).: IEEE Comput. Soc. Press.

Kanehira, N., Kawasaki, T., Ohta, S., Ismumi, T., Kawada, T., Kanehiro, F., Kajita, S., & Kaneko, K. (2002). Design and experiments of advanced leg module (HRP-2L) for humanoid robot (HRP-2) development. In *IEEE/RSJ International Conference on Intelligent Robots and System*, volume 3 (pp. 2455–2460).: IEEE.

Kaneko, K., Harada, K., Kanehiro, F., Miyamori, G., & Akachi, K. (2008). Humanoid robot HRP-3. In *2008 IEEE/RSJ International Conference on Intelligent Robots and Systems* (pp. 2471–2478).: IEEE.

Kang, K. I., Freedman, S., Matarić, M. J., Cunningham, M. J., & Lopez, B. (2005). A hands-off physical therapy assistance robot for cardiac patients. *Proc. 2005 IEEE 9th Int. Conf. Rehabil. Robot.*, 2005, 337–340.

Kato, I., Kakuo, M., Hirabayashi, H., Ishihara, Y., Endo, T., & Kohinata, S. (1973). Feet: Humanoid hydraulic walking machine (development of biped robot (WABOT-1))). *Biomechanisms*, 2, 175–184.

Kim, J.-H. & Oh, J.-H. (2004). Walking control of the humanoid platform KHR-1 based on torque feedback control. In *IEEE International Conference on Robotics and Automation, 2004. Proceedings. ICRA '04. 2004.*, volume 1 (pp. 623–628 Vol.1).

Kim, J. H., Park, S. W., Park, I. W., & Oh, J. H. (2002). Development of a humanoid biped walking robot platform KHR-1 initial design and its performance evaluation. *Proceedings of 3rd IARP International Workshop on Humanoid and Human Friendly Robotics*, 1(January), 12.

Ko, A. & Lau, H. Y. K. (2009). Robot assisted emergency search and rescue system with a wireless sensor network. *Int. J. Adv. Sci. Technol.*, 3, 69–78.

Kormushev, P., Ugurlu, B., Calinon, S., Tsagarakis, N. G., & Caldwell, D. G. (2011). Bipedal walking energy minimization by reinforcement learning with evolving policy parameterization. In *2011 IEEE/RSJ International Conference on Intelligent Robots and Systems* (pp. 318–324).

Kuindersma, S., Deits, R., Fallon, M., Valenzuela, A., Dai, H., Permenter, F., Koolen, T., Marion, P., & Tedrake, R. (2016). Optimization-based locomotion planning, estimation, and control design for the Atlas humanoid robot. *Auton. Robots*, 40(3), 429–455.

Kuindersma, S., Permenter, F., & Tedrake, R. (2014). An efficiently solvable quadratic program for stabilizing dynamic locomotion. In *2014 IEEE Int. Conf. Robot. Autom.* (pp. 2589–2594).: IEEE.

Lee, D.-W., Lee, M.-J., & Kim, M.-S. (2015). Whole body imitation of human motion with humanoid robot via ZMP stability criterion. In *2015 IEEE-RAS 15th International Conference on Humanoid Robots (Humanoids)*, volume 2015-Decem (pp. 1003–1006).: IEEE.

Lim, H.-o. & Takanishi, A. (2007). Biped walking robots created at Waseda University: WL and WABIAN family. *Philosophical Transactions of the Royal Society A: Mathematical, Physical and Engineering Sciences*, 365(1850), 49–64.

Lundberg, U., Granqvist, M., Hansson, T., Magnusson, M., & Wallin, L. (1989). Psychological and physiological stress responses during repetitive work at an assembly line. *Work Stress*, 3(2), 143–153.

Marinho, M. M., Adorno, B. V., Harada, K., & Mitsuishi, M. (2019). Dynamic Active Constraints for Surgical Robots Using Vector-Field Inequalities. *IEEE Trans. Robot.*, 35(5), 1166–1185.

Maximo, M. R. O. A., Ribeiro, C. H. C., & Afonso, R. J. M. (2016). Mixed-integer programming for automatic walking step duration. In *2016 IEEE/RSJ Int. Conf. Intell. Robot. Syst.*, volume 2016-Novem (pp. 5399–5404).: IEEE.

McGeer, T. (1988). Stability and control of two-dimensional biped walking. *Center for Systems Science, Simon Fraser University, Burnaby, BC, Canada, Technical Report*, 1.

McGeer, T. (1990a). Passive bipedal running. *Proceedings of the Royal Society of London. B. Biological Sciences*, 240(1297), 107–134.

McGeer, T. (1990b). Passive walking with knees. In *Proceedings., IEEE International Conference on Robotics and Automation* (pp. 1640–1645).: IEEE.

McGeer, T. (1993). Dynamics and control of bipedal locomotion. *Journal of theoretical biology*, 163(3), 277–314.

McGeer, T. et al. (1990). Passive dynamic walking. *Int. J. Robotics Res.*, 9(2), 62–82.

Metta, G., Natale, L., Nori, F., Sandini, G., Vernon, D., Fadiga, L., von Hofsten, C., Rosander, K., Lopes, M., Santos-Victor, J., Bernardino, A., & Montesano, L. (2010). The iCub humanoid robot: An open-systems platform for research in cognitive development. *Neural Networks*, 23(8-9), 1125–1134.

Moran, M. E. (2006). The da Vinci Robot. *Journal of Endourology*, 20(12), 986–990.

Moran, M. E. (2007). Evolution of robotic arms. *J. Robot. Surg.*, 1(2), 103–111.

Mori, M., MacDorman, K. F., & Kageki, N. (2012). The uncanny valley. *IEEE Robot. Autom. Mag.*, 19(2), 98–100.

Murphy, T., Naugle, D. E., Eardley, R., Maestas, J. D., Griffiths, T., Pellant, M., & Stiver, S. J. (2013). Trial by Fire. *Rangelands*, 35(3), 2–10.

Nagaoka, K., Kubota, T., Otsuki, M., & Tanaka, S. (2008). Experimental study on autonomous burrowing screw robot for subsurface exploration on the Moon. In *2008 IEEE/RSJ Int. Conf. Intell. Robot. Syst.* (pp. 4104–4109).: IEEE.

Naveau, M., Kudruss, M., Stasse, O., Kirches, C., Mombaur, K., & Souères, P. (2017). A Reactive Walking Pattern Generator Based on Nonlinear Model Predictive Control. *IEEE Robot. Autom. Lett.*, 2(1), 10–17.

Nelson, G., Saunders, A., Neville, N., Swilling, B., Bondaryk, J., Billings, D., Lee, C., Playter, R., & Raibert, M. (2012). PETMAN: A Humanoid Robot for Testing Chemical Protective Clothing. *Journal of the Robotics Society of Japan*, 30(4), 372–377.

Newcome, L. R. (2004). *Unmanned Aviation: A Brief History of Unmanned Aerial Vehicles*. Reston ,VA: American Institute of Aeronautics and Astronautics.

Nishiwaki, K., Kuffner, J., Kagami, S., Inaba, M., & Inoue, H. (2007). The experimental humanoid robot H7: a research platform for autonomous behaviour. *Philosophical Transactions of the Royal Society A: Mathematical, Physical and Engineering Sciences*, 365(1850), 79–107.

Nishiwaki, K., Sugihara, T., Kagami, S., Kanehiro, F., Inaba, M., & Inoue, H. (2000). Design and development of research platform for perception-action integration in humanoid robot: H6. In *Proceedings. 2000 IEEE/RSJ International Conference on Intelligent Robots and Systems (IROS 2000) (Cat. No.00CH37113)*, volume 3 (pp. 1559–1564).: IEEE.

Oliveira, A. C. (2015). Gait and Balance Kinematic Control for a Humanoid Robot Based on Dual Quaternion Algebra. (pp. 134).

Oliveira, A. C. & Adorno, B. V. (2015). Balance Control of a Humanoid Robot Based on the Cooperative Dual Task-space Framework. *XII Simpósio Bras. Automação Intel.*, (pp. 485–490).

Pasek, A. (2014). Renaissance Robotics: Leonardo da Vinci's Lost Knight and Enlivened Materiality. *Grad. J. Vis. Mater. Cult. Issue*, (7), 1–25.

Pratt, J., Chew, C.-M., Torres, A., Dilworth, P., & Pratt, G. (2001). Virtual model control: An intuitive approach for bipedal locomotion. *The International Journal of Robotics Research*, 20, 129–143.

Quiroz-Omana, J. J. & Adorno, B. V. (2019). Whole-Body Control With (Self) Collision Avoidance Using Vector Field Inequalities. *IEEE Robotics and Automation Letters*, 4(4), 4048–4053.

Radford, N. A., Strawser, P., Hambuchen, K., Mehling, J. S., Verdeyen, W. K., Donnan, A. S., Holley, J., Sanchez, J., Nguyen, V., Bridgwater, L., Berka, R., Ambrose, R., Myles Markee, M., Fraser-Chanpong, N. J., McQuin, C., Yamokoski, J. D., Hart, S., Guo, R., Parsons, A., Wightman, B., Dinh, P., Ames, B., Blakely, C., Edmondson, C., Sommers,

B., Rca, R., Tobler, C., Bibby, H., Howard, B., Niu, L., Lee, A., Conover, M., Truong, L., Reed, R., Chesney, D., Platt, R., Johnson, G., Fok, C.-L., Paine, N., Sentis, L., Cousineau, E., Sinnet, R., Lack, J., Powell, M., Morris, B., Ames, A., & Akinyode, J. (2015). Valkyrie: NASA's First Bipedal Humanoid Robot. *Journal of Field Robotics*, 32(3), 397–419.

Raibert, M., Blankespoor, K., Nelson, G., & Playter, R. (2008). BigDog, the Rough-Terrain Quadruped Robot. *IFAC Proc. Vol.*, 41(2), 10822–10825.

Raibert, M. H. (1984). Hopping in legged systems - modeling and simulation for the two-dimensional one-legged case. *IEEE Transactions on Systems, Man, and Cybernetics*, (3), 451–463.

Raibert, M. H. (1986). Legged robots that balance. *Communications of the ACM*, 29(6), 499–514.

Reher, J. & Ames, A. D. (2021). Dynamic walking: Toward agile and efficient bipedal robots. *Annual Review of Control, Robotics, and Autonomous Systems*, 4, 535–572.

Rohmer, E., Singh, S. P. N., & Freese", M. (2013). "CoppeliaSim (formerly V-REP): a Versatile and Scalable Robot Simulation Framework". In *"Proc. of The International Conference on Intelligent Robots and Systems (IROS)"*. www.coppeliarobotics.com.

Sales, J., Martí, J. V., Marín, R., Cervera, E., & Sanz, P. J. (2016). CompaRob: The Shopping Cart Assistance Robot. *Int. J. Distrib. Sens. Networks*, 12(2), 4781280.

Schwind, W. J. & Koditschek, D. (2000). Approximating the stance map of a 2-dof monoped runner. *Journal of Nonlinear Science*, 10, 533–568.

Siegwart, R., Nourbakhsh, I., & Scaramuzza, D. (2004). Introduction to autonomous mobile robots.

Spong, M. & Bullo, F. (2005). Controlled symmetries and passive walking. *IEEE Transactions on Automatic Control*, 50, 1025–1031.

Spong, M. W., Hutchinson, S., & Vidyasagar, M. (2006). *Robot Modeling and Control*. New York: Wiley.

Tarokh, M., McDermott, G., Hayati, S., & Hung, J. (1999). Kinematic modeling of a high mobility Mars rover. In *Proc. 1999 IEEE Int. Conf. Robot. Autom. (Cat. No.99CH36288C)*, volume 2 (pp. 992–998).: IEEE.

Tedrake, R., Zhang, T., fai Fong, M., & Seung, H. (2004). Actuating a simple 3d passive dynamic walker. In *IEEE International Conference on Robotics and Automation, 2004. Proceedings. ICRA '04. 2004.*, volume 5 (pp. 4656–4661 Vol.5).

Todd, D. J. (1985). *Walking Machines - An Introduction to Legged Robots.* Boston, MA: Springer US.

Urban, S. D. & Adorno, B. V. (2019). Constraint-based Gait Control Using Differential Inequalities. *Work. Appl. Dual Quaternion Algebr. to Robot.*, (pp. 1–2).

Vidoni, R. & Gasparetto, A. (2011). Efficient force distribution and leg posture for a bio-inspired spider robot. *Rob. Auton. Syst.*, 59(2), 142–150.

Volpe, R., Balaram, J., Ohm, T., & Ivlev, R. (1996). Rocky 7: a next generation Mars rover prototype. *Adv. Robot.*, 11(4), 341–358.

VUKOBRATOVIĆ, M. & BOROVAC, B. (2004). ZERO-MOMENT POINT - THIRTY FIVE YEARS OF ITS LIFE. *Int. J. Humanoid Robot.*, 01(01), 157–173.

Vukobratović, M., Borovac, B., & Potkonjak, V. (2006). ZMP: A REVIEW OF SOME BASIC MISUNDERSTANDINGS. *Int. J. Humanoid Robot.*, 03(02), 153–175.

Vukobratovic, M. & Juricic, D. (1969). Contribution to the Synthesis of Biped Gait. *IEEE Trans. Biomed. Eng.*, BME-16(1), 1–6.

Westervelt, E., Grizzle, J., Chevallereau, C., Choi, J. H., & Moris, B. (2018). *Feedback Control of Dynamic Bipedal Robot Locomotion.* CRC Press.

Westervelt, E., Grizzle, J., & Koditschek, D. (2003). Hybrid zero dynamics of planar biped walkers. *IEEE Transactions on Automatic Control*, 48, 42–56.

Whitcomb, L., Yoerger, D. R., Singh, H., & Howland, J. (2000). Advances in Underwater Robot Vehicles for Deep Ocean Exploration: Navigation, Control, and Survey Operations. In *Robot. Res.* (pp. 439–448). London: Springer London.

Wiedebach, G., Bertrand, S., Wu, T., Fiorio, L., McCrory, S., Griffin, R., Nori, F., & Pratt, J. (2016). Walking on partial footholds including line contacts with the humanoid robot Atlas. In *2016 IEEE-RAS 16th International Conference on Humanoid Robots (Humanoids)* (pp. 1312–1319).: IEEE.

Wilcox, B. H., Litwin, T., Biesiadecki, J., Matthews, J., Heverly, M., Morrison, J., Townsend, J., Ahmad, N., Sirota, A., & Cooper, B. (2007). Athlete: A cargo handling and manipulation robot for the moon. *J. F. Robot.*, 24(5), 421–434.

Yoerger, D., Bradley, A., Walden, B., Cormier, M.-H., & Ryan, W. (2000). Fine-scale seafloor survey in rugged deep-ocean terrain with an autonomous robot. In *Proc. 2000 ICRA. Millenn. Conf. IEEE Int. Conf. Robot. Autom. Symp. Proc. (Cat. No.00CH37065)*, volume 2 (pp. 1787–1792).: IEEE.

Yokoi, K., Kanehiro, F., Kaneko, K., Kajita, S., Fujiwara, K., & Hirukawa, H. (2004). Experimental Study of Humanoid Robot HRP-1S. *The International Journal of Robotics Research*, 23(4-5), 351–362.

Yoshida, E. (2018). Robots that look like humans: A brief look into humanoid robotics. *Mètode Rev. difusió la Investig.*, 2019(9), 143–151.